High-content live-cell imaging reveals co-regulation of cardiomyocyte decisions of hypertrophy and apoptosis

Bryan Chun[1], Jeffrey J. Saucerman[1]*

[1]Department of Biomedical Engineering and Robert M. Berne Cardiovascular Research Center, University of Virginia, Charlottesville, VA 22908,USA

*Lead contact: jsaucerman@virginia.edu

Abstract

Cardiomyocyte hypertrophy and apoptosis underlie cardiomyopathies and heart failure. While previous studies have described hypertrophy or apoptosis at the level of cell populations, how individual cells commit to these distinct yet co-regulated fates is unclear. We used high-content imaging to track single-cell hypertrophy and apoptosis dynamics, revealing new features and unique subpopulation responses. Catecholamines isoproterenol and norepinephrine induced heterogeneous analog hypertrophy and digital apoptosis, which support a “grow and/or die” conceptual model for cell decisions. Multinomial log-linear models indicated that a cell’s initial size and DNA content predict its susceptibility to hypertrophy and apoptosis. This work integrates dynamic morphological and biochemical cell profiling to reveal that cardiomyocyte hypertrophic and apoptotic responses to catecholamines represent an incoherent feedforward loop in which hypertrophy enhances survival.

Introduction

Cells utilize a finite number of signaling pathways and intermediates to determine a multitude of cell fates such as developmental specification (Nüsslein-Volhard and Wieschaus, 1980; Petkova et al., 2019) or drug responses (Behar et al., 2013, 2007; Greenwald et al., 2013; Saucerman and McCulloch, 2006). For example, heart failure involves both cardiomyocyte hypertrophy and apoptosis (Frey et al., 2004; Levy et al., 1990; Ryall et al., 2012; Wencker et al., 2003). While apoptosis has been clearly implicated in heart failure progression (Wencker et al., 2003) , hypertrophy can be physiological or pathological (Dorn, 2007; Sano et al., 2007). Furthermore, apoptosis and hypertrophy may have interacting roles that result in the transition from physiological to pathological hypertrophy. These interactions need to be better understood to develop targeted therapeutic strategies for heart failure (Owens, 2005).

A number of studies have shown that cardiomyocyte hypertrophy and apoptosis are co-regulated *in vivo*. For example, pressure-overload and catecholamine overstimulation induce both hypertrophy and apoptosis (Engelhardt et al., 1999; Shizukuda et al., 1998; Teiger et al., 1996), while calcineurin overexpression elicits hypertrophy protective against apoptosis [14] even as calcineurin itself directly dephosphorylates the pro-apoptotic Bcl-2 family protein BAD (Springer et al., 2000; Wang et al., 1999). However, *in vivo* studies do not elucidate the dynamic, functional relationships between hypertrophy and apoptosis at the level of single cells. As such, it is unclear whether hypertrophy and apoptosis decisions occur concurrently, sequentially, or in opposition to each other (Kang et al., 2015; van Empel and De Windt, 2004).

As the field lacks a conceptual model, we identify three possible conceptual models for joint cardiomyocyte decision-making of hypertrophy and apoptosis. A “grow-and-die” model suggests serial decision-making where cells hypertrophy but then later apoptose due to an inability to handle growth stresses (Sawyer et al., 2002). The importance of caspase activation dynamics as

46 a regulator of apoptosis and the role of sub-apoptotic caspase activity in hypertrophy suggests a
47 distinct "grow-or-die" model, in which caspase activation dynamics regulate whether
48 cardiomyocytes will either survive and hypertrophy or die prior to hypertrophic growth
49 (Putinski et al., 2013; Roux et al., 2015). An alternative to these previously implicated
50 conceptual models is a "grow-and/or-die" model, which suggests that mixtures of different
51 subpopulations of cells undergo both possibilities. In this model, a stimulus may induce a
52 subpopulation of cells to undergo hypertrophy. While this response may be protective against
53 apoptosis, hypertrophic cells may also reach a physical limit of viability and subsequently
54 undergo apoptosis. Fixed timepoint *in vivo* experiments cannot determine which of these three
55 conceptual models is most likely to be occurring dynamically and at a single-cell level. *In vitro*
56 studies of isolated cardiomyocytes have examined hypertrophy (Morisco et al., 2001; Ryall et al.,
57 2014; Vidal et al., 2012) or apoptosis (Iwai-Kanai et al., 1999; Saito et al., 2000; Shin et al.,
58 2014) independently. To our knowledge, however, co-regulation of hypertrophy and apoptosis
59 has not been examined simultaneously in isolated cardiomyocytes. Understanding the
60 differential co-regulation of hypertrophy and apoptosis is critical to differentiate between
61 pathological hypertrophy, which is accompanied by apoptosis, and compensatory hypertrophy
62 in the absence of apoptosis (D'Angelo et al., 1997; Grossman et al., 1975; Hayakawa et al., 2003;
63 van Empel and De Windt, 2004).

64 Adrenergic catecholamine signaling is a key target in the treatment of heart failure as it
65 promotes both cardiomyocyte hypertrophy and apoptosis. Fixed-end point techniques have
66 demonstrated that cardiomyocyte hypertrophy induced by catecholamines requires sub-
67 apoptotic levels of caspase activation (Putinski et al., 2013). However, end point or cell lysis
68 assays do not capture initial heterogeneity, which may provide predictive or explanatory factors
69 for different phenotypes. Dynamic time course data is necessary to elucidate the mechanisms by
70 which individual cells decide to grow or die, and the interaction between those decisions (Paek
71 et al., 2016; Roux et al., 2015). To overcome these limitations, here, we designed a live-cell high-

content imaging approach that monitors the dynamics of growth and death simultaneously at a single-cell level. This approach incorporates multiplexed measurements of multiple phenotypes to understand the relationship between hypertrophy and apoptosis; dynamic time course measurements to elucidate the mechanisms by which individual cells decide to grow or die; the interaction between those decisions; and single-cell measurements of decision-making.

Here, we characterize the cellular, nuclear, and biochemical single-cell dynamic hypertrophy and apoptosis responses of cardiomyocytes to multiple perturbations. We identify a biphasic cardiomyocyte concentration response to the catecholamine isoproterenol, resulting from opposing digital apoptosis and analog hypertrophy responses. Classification of cell responses into that of three subpopulations reveals differential concentration-dependent dynamic responses. Finally, a multinomial log-linear data-driven model reveals new characteristics of a cell that predicts its likelihood of committing to hypertrophy or apoptosis, which we then validate. Our work thus develops a common experimental and statistical framework to reveal signaling and phenotypic dynamics that underlie individual cell decision-making.

Results

Assay design for single-cell phenotyping of hypertrophy-apoptosis dynamics

Our live single-cell assay uses multiple simultaneous fluorescent readouts of hypertrophic and apoptotic activity (**Figure 1A**). Cells were transduced with eGFP as a live-cell reporter of single-cell morphology and protein synthesis. Nuclei were labeled with Hoechst, and general cell death and apoptosis were measured with propidium iodide (PI) and fluorescently-conjugated annexin V (A5). To track temporal dynamics, individual wells in a 96-well microplate representing different treatment conditions were imaged for 48 hours with a 1 hour resolution (**Figure 1B**).

95 After live-cell imaging, cells were fixed, permeabilized, and immunostained to detect cardiomyocyte-
96 specific α-actinin expression. We developed automated image analysis methods to measure dynamics of
97 multiple metrics related to cellular morphology, viability, and final α-actinin expression at a single-cell
98 level (**Methods**).

99 To correct for cell-to-cell eGFP expression variability and uneven fluorescence that persisted
100 after flatfield illumination, we trained a random forest classifier to generate probability maps of
101 eGFP (**Figure 1C**). The random forest model was robust to at least a 5-fold range in variations
102 in fluorescence signal-to-noise ratio, allowing optimization of fluorescence acquisition settings
103 to minimize phototoxicity (**Supplemental Figure 1**). We used this eGFP probability map for
104 thresholding, single-cell segmentation, and tracking for longitudinal morphology and
105 fluorescence measurements (**Figure 1D** and **Methods**). As our eGFP reporter was expressed
106 under a ubiquitous CMV promoter and thus could not differentiate between cardiomyocytes and
107 other cell types, we used an α-actinin fixed immunofluorescence probability map and live single-
108 cell tracking to identify cardiomyocytes. Similarly, a live A5 probability map was used to
109 determine A5 positivity of each cell.

110 This assay was validated using cells treated with DMSO as a negative vehicle control. Even in the
111 absence of hypertrophic or apoptotic stimuli, cells showed a wide range of both hypertrophic
112 (**Figure 1A** and **D**, orange outline and traces) and apoptotic trajectories (cyan outline and
113 traces). At the cell-population level, we found that A5 binding accumulated earlier than PI
114 uptake, suggesting that most of the death observed was due to apoptosis rather than other death
115 processes (**Figure 1F**). This apoptotic lag between initial A5 binding and later PI uptake at the
116 population level was validated in individual A5/PI double-positive cells (**Figure 1G**).

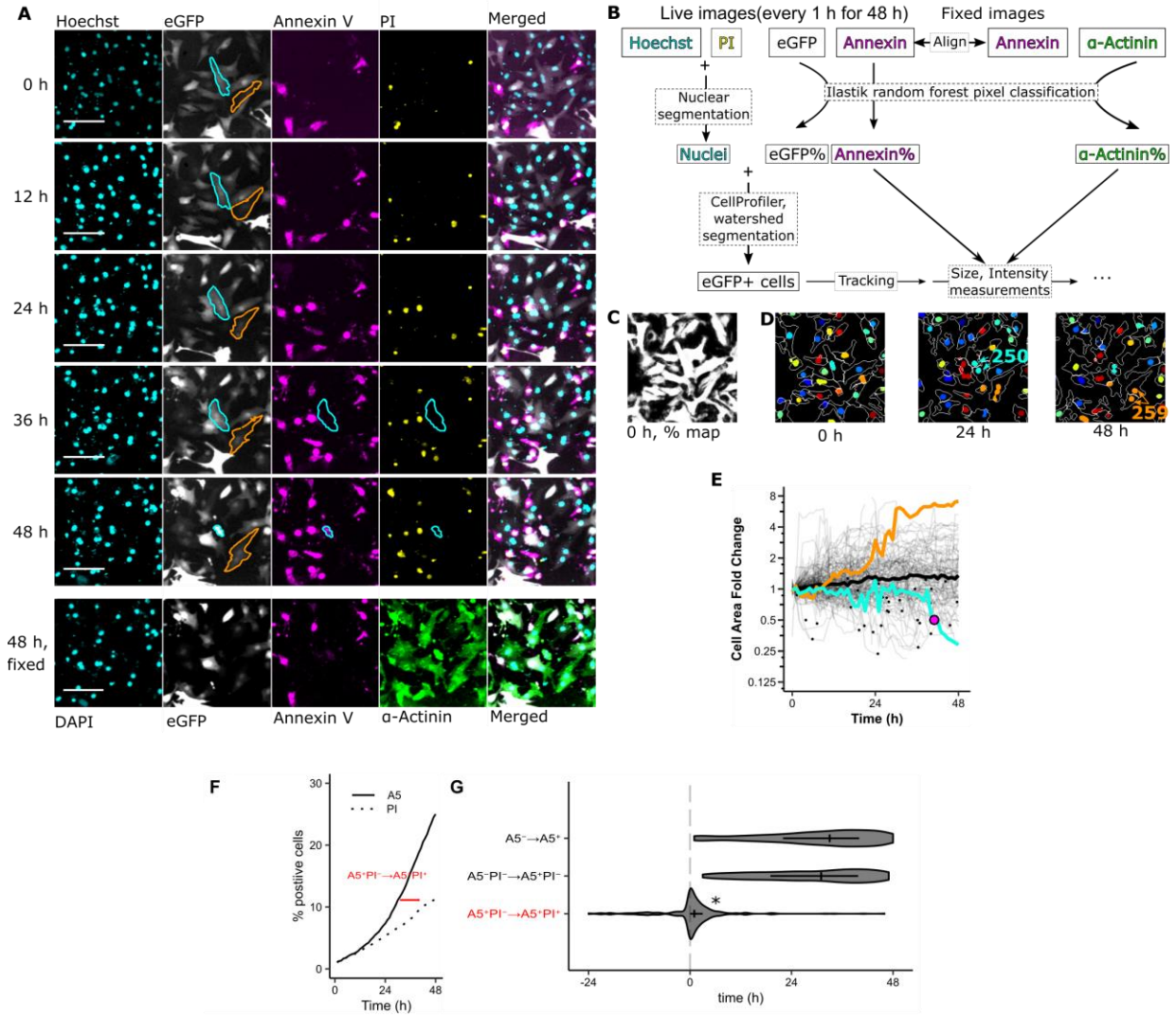

Figure 1. High-content time-lapse microscopy of single-cell morphological and apoptosis dynamics of neonatal rat cardiac myocytes.

(**A**) Representative timelapse images of neonatal rat cardiac cells treated with 0.1% DMSO (neg. control). Live imaging tracked changes in morphology of eGFP-expressing cells and apoptotic A5 and PI binding over 48 hours (rows 1 through 5). After two days (row 6), cells were fixed and stained for DNA (DAPI, cyan) and α-actinin (green). Outlines represent manual segmentation of cells undergoing hypertrophy (orange) or early apoptotic A5 binding and PI exclusion (cyan). Scale bar is 100 µm.

(**B**) Schematic of image analysis pipeline for single-cell cardiomyocyte hypertrophy and apoptosis dynamics.

(**C**) Example eGFP fluorescence probability map for the GFP image in (A) for image thresholding and segmentation.

(**D**) Example segmentation and tracking of cells in (A). White outlines represent automated segmentation results of eGFP cells and pseudocoloured ovals represent nuclear segmentation. The tracking of the two outlined cells in (A) are marked with their identifier (cyan and orange numbers and arrows).

134 (**E**) Single-cell heterogeneity in cardiomyocyte hypertrophy dynamics (black lines). Orange and
135 cyan traces correspond to previously identified cells. Solid black line corresponds to the
136 population median. Black dots indicate onset of A5 binding as does the large magenta dot for the
137 cyan trace. Cell Area Fold Change reported as cell areas normalized to the average of areas
138 measured at initial two timepoints.
139 (**F**) Empirical cumulative distribution function of A5 (magenta) and PI (yellow) binding for all
140 DMSO-treated cells. The rightward shift of the PI binding curve indicates later onset of PI
141 binding in the cell population suggestive of apoptosis.
142 (**G**). Single-cell quantification of onset of A5 and PI binding show that PI occurs after A5 binding
143 , with the lag between those two events quantified (red distribution; * $p = 0.019$, one-sample
144 Wilcoxon signed rank test, $n = 733$ cells).
145

146 ***Cellular and nuclear profiling of staurosporine-induced apoptosis dynamics***

147 Apoptosis is characterized by morphological and biochemical changes to both cell and nucleus.
148 As a representative cellular perturbation to examine apoptosis dynamics with our high-content
149 imaging assay, we selected stimulation with staurosporine (STS), an ATP-competitive inhibitor
150 with activity against a broad spectrum of kinases and a well-known inducer of apoptosis in
151 multiple cell types including cardiomyocytes (Belmokhtar et al., 2001; Lawrie et al., 1997;
152 Meggio et al., 1995; Yue et al., 1998). Apoptotic or death markers such as A5 or PI are routinely
153 used in flow cytometry and STS apoptosis dynamics have been characterized in cardiomyocytes
154 at a coarse time resolution at the population level (Wlodkowic et al., 2009; Yue et al., 1998). Our
155 high-content imaging assay uniquely allows for simultaneous characterization and high-
156 resolution dynamic single-cell tracking of multiple features related to apoptosis including A5
157 binding, PI uptake, changes in nuclei morphology, and chromatin condensation and
158 degradation.

159 Treatment with STS induced large amounts of cell death marked by increased A5 binding and PI
160 uptake compared to DMSO vehicle-control treatment (**Figure 2A** and **B**). Bulk-population
161 dynamics of total accumulation of A5 and PI were again suggestive of apoptosis, with PI-uptake
162 occurring later than that of A5 (**Figure 2C**). However, the dynamics of apoptosis were markedly

163 different between STS and DMSO treatments. DMSO treatment induced a biphasic response
164 with initially low levels of A5 and PI binding between 0 and 24 hours and a second phase of
165 increased apoptotic activity after 24 hours. In contrast, STS-treated cells largely completed
166 apoptosis within the first 36 hours of treatment. There was a significant lag from A5 to PI
167 binding in single cells that eventually became A5/PI-double positive (**Figure 2D**), suggesting
168 apoptosis and not other forms of cell death.

169 Next, we sought to characterize the temporal dynamics of additional cellular features that may
170 be associated with apoptosis (**Figure 2E**). As expected, STS treatment induced global increases
171 of cell membrane A5 binding followed by nuclear PI uptake. Motivated by known apoptotic
172 nuclear and chromatin changes (Toné et al., 2007), we also investigated dynamic changes in
173 nuclear Hoechst staining. Mean, total (integrated), and median absolute deviation of the
174 Hoechst intensity all followed similar trajectories, with STS-treated trajectories increasing above
175 the DMSO-treated baseline, reflecting increased membrane permeability to Hoechst and
176 chromatin condensation (Ormerod et al., 1993). After approximately 24 hours, STS-treated
177 trajectories of Hoechst decreased below that of DMSO-treated trajectories, suggesting DNA
178 degradative apoptotic processes. We also investigated changes in nuclear morphology. During
179 the first 36 hours, nuclei of STS-treated cells had smaller nuclei, which later increased in size
180 relative to their DMSO-treated counterparts. Interestingly, nuclear form factor decreased and
181 eccentricity increased in STS-treated cells relative to DMSO-treated cells even at the very early
182 times, indicating more irregular and less circular nuclei consistent with apoptosis. Overall, these
183 analyses delineate a temporal sequence of apoptotic kinetics, starting with changes to nuclear
184 permeability and shape, followed by A5 binding, and finally loss of cell membrane integrity.

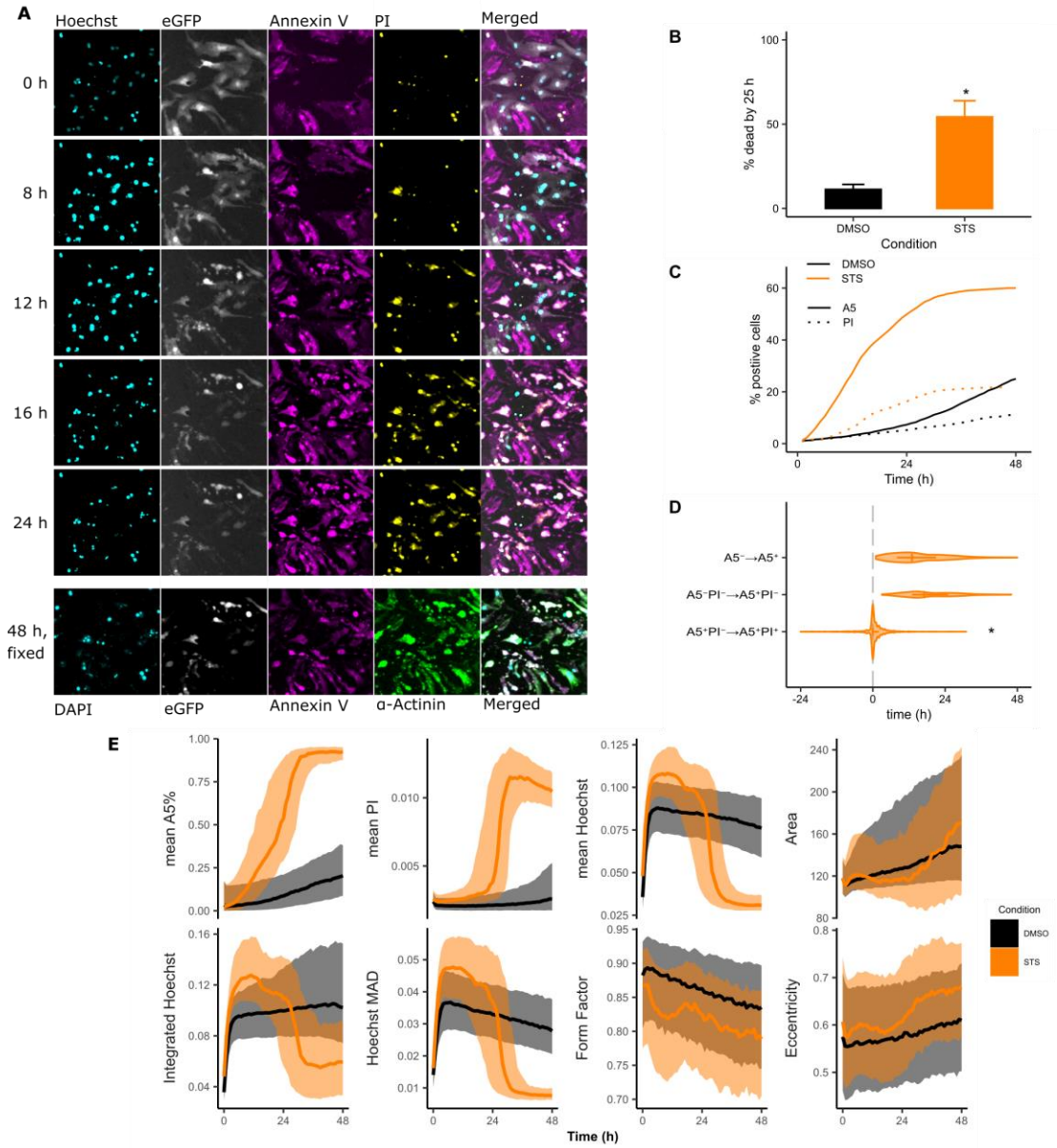

Figure 2. Single-cell dynamics of cardiomyocyte death induced by staurosporine. (**A**) Representative timelapse images of neonatal rat cardiac cells treated with 1 µM STS show induction of A5 and PI binding (magenta and yellow, respectively) and pyknosis (cyan). (**B**) 1 µM STS increased the fraction of dead (either A5-or PI-positive) cells compared to the 0.1% DMSO vehicle control condition (* p = 0.036, paired Welch's one-tailed *t*-test n = 2 independent cell isolations). (**C**) Empirical cumulative distribution function of A5 (magenta) and PI (yellow) binding for all STS-treated cells. Same DMSO traces as in **Figure 1F**. (**D**) Single-cell quantification of onset of A5 and PI binding show that PI occurs after A5 binding (red, with the lag between those two events quantified (red distribution; * p = 0.01894, one-sample Wilcoxon signed rank test, n = 733 cells).

197 (**E**) Single-cell dynamics of nuclear metrics in response to either 1 μM STS or 0.1% DMSO
198 control. Solid lines indicate population median, shaded areas indicate interquartile range.
199
200
201 ***Cellular profiling of phenylephrine-induced hypertrophy dynamics***

202 To examine hypertrophy dynamics with our high-content imaging assay, we selected stimulation with
203 the catecholamine phenylephrine (PE), an α1-adrenergic agonist and a well-known inducer of
204 cardiomyocyte hypertrophy (O'Connell et al., 2003; Ryall and Saucerman, 2012). Cardiac α1-
205 adrenergic signaling is thought to be cardioprotective by activating cell survival signaling pathways
206 (Iwai-Kanai et al., 1999; O'Connell et al., 2014). We also examined the protein translation
207 inhibitor cycloheximide (CHX) as an additional negative control to control for baseline protein
208 synthesis (Schneider-Poetsch et al., 2010).

209 Treatment with PE induced hypertrophy and a striking increase in eGFP expression, consistent
210 with known increases in protein synthesis (**Figure 3A-C**). The greatest increase in median cell
211 areas relative to DMSO occurred around 24 h (**Figure 3D**). Interestingly, there was a wide
212 distribution in single-cell changes in area. Comparison of the empirical cumulative distribution
213 functions (eCDFs) of the DMSO- and PE-treated cells show not simply a rightward shift in
214 distribution when cells are treated with a hypertrophic agonist, but rather an increase in the
215 upper tail of distribution of cell areas (**Figure 3F**). This indicates that population-level
216 increases in cell area seen with PE treatment is due to a subpopulation of hypertrophic
217 responders as opposed to global increases in cell area. PE treatment increased the proportion of
218 hypertrophic responders, or cells with fold change areas greater than that of the 75th percentile
219 of DMSO, while CHX treatment reduced this proportion (**Figure 3G**).

220 We previously identified divergent characteristics of cellular hypertrophy induced by different
221 hypertrophic agonists (Bass et al., 2012). While our previous approach segmented on α-actinin
222 immunofluorescence, here we find greater fidelity when further incorporating cell-to-cell variation in

223 eGFP expression (**Supplemental Figure 2**). We therefore re-characterized the same metrics of
224 cell shape and size and found that treatment with PE led to significant changes to all metrics
225 observed (**Figure 3H**). As expected, PE increased raw cell area and major axis length.
226 Elongation (axis ratio), eccentricity, and form factor all decreased, suggesting PE-treated cells
227 became more circular but more spiky (**Figure 3A**, red outline).

228 Previous reports have suggested a role for increased DNA synthesis and polyploidy in cardiac
229 hypertrophy, and we recently published a method for determining cardiomyocyte nuclear ploidy
230 with the nuclear stain DAPI (Liu et al., 2010; Woo et al., 2019). Further, Hoechst has been
231 shown to be a reliable marker for chromatin compaction, which may play a functional role in
232 transcription (Imai et al., 2017). We therefore asked whether the hypertrophic stimulus PE also
233 affected nuclear characteristics as measured by Hoechst. While nuclear morphological
234 characteristics remained unchanged, we found that PE-treated cells initially took up less
235 Hoechst than DMSO-treated counterparts but finished with an overall brighter Hoechst signal,
236 suggesting increased DNA content (**Figure 3I**). The smaller initial Hoechst intensity may
237 reflect more robust nuclear membrane integrity due to the cell survival signaling pathways
238 activated by PE and the relative rates of phospholipid turnover and DNA synthesis (Homa et al.,
239 1991; Rew and Wilson, 2000).

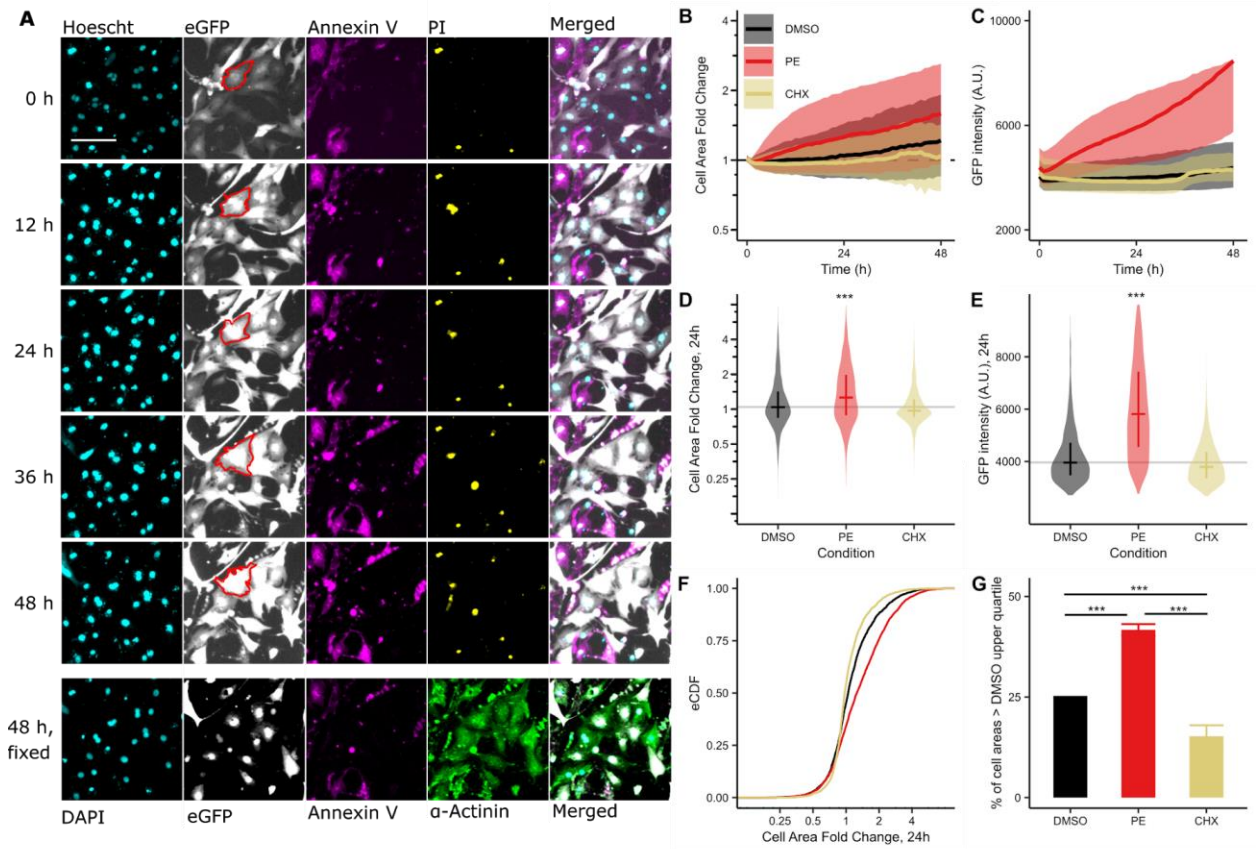
A
Hoescht
eGFP
Annexin V
PI
Merged
0 h
12 h
24 h
36 h
48 h
48 h, fixed
DAPI
eGFP
Annexin V
α-Actinin
Merged
B
DMSO
PE
CHX
Cell Area Fold Change
Time (h)
C
GFP intensity (A.U.)
Time (h)
D
Cell Area Fold Change, 24h
Condition
E
GFP intensity (A.U.), 24h
Condition
F
eCDF
Cell Area Fold Change, 24h
G
% of cell areas > DMSO upper quartile

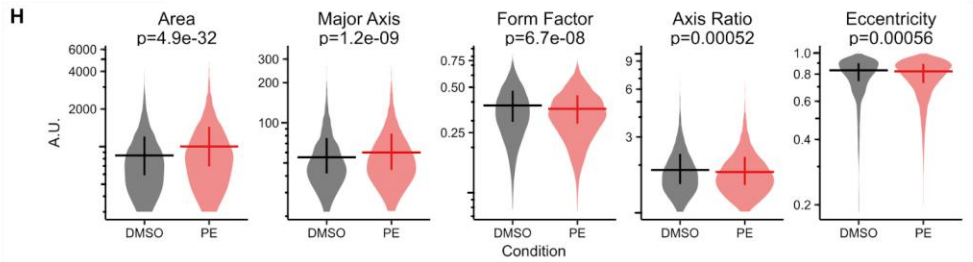
H
Area
p=4.9e-32
Major Axis
p=1.2e-09
Form Factor
p=6.7e-08
Axis Ratio
p=0.00052
Eccentricity
p=0.00056
A.U.
DMSO
PE
Condition

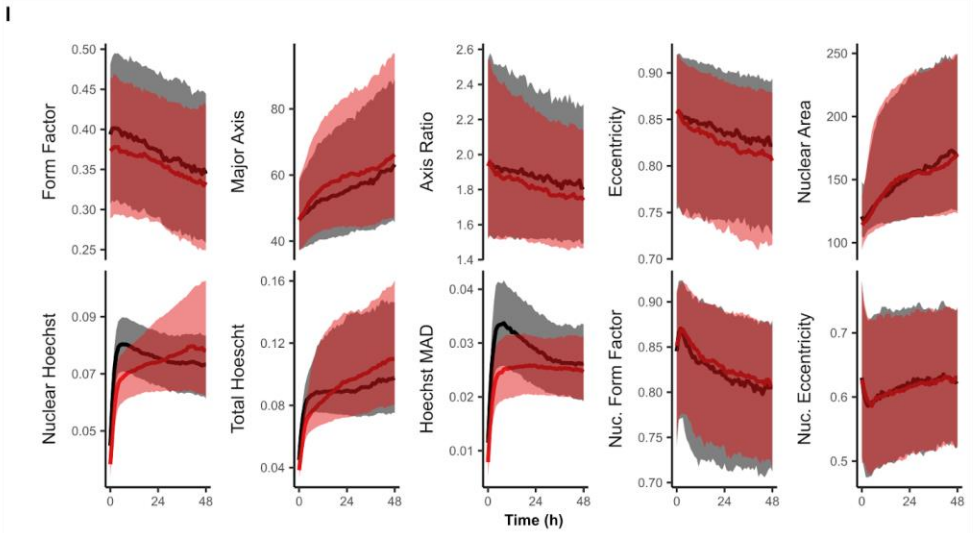
I
Form Factor
Major Axis
Axis Ratio
Eccentricity
Nuclear Area
Nuclear Hoechst
Total Hoescht
Hoechst MAD
Nuc. Form Factor
Nuc. Eccentricity
Time (h)

240

Figure 3. Single-cell dynamics of cardiomyocyte hypertrophy in response to phenylephrine.

(**A**) Representative timelapse images of neonatal rat cardiac cells treated with 50 μM PE showing induction of hypertrophy (red outline) and eGFP expression (gray).

48h hypertrophy dynamics (**B**) and eGFP dynamics (**C**) of cells treated with 50 μM PE, 50 μM CHX, or 0.1% DMSO vehicle control. Solid lines indicate population median, shaded areas indicate interquartile range.

24h treatment with 50μM PE induces hypertrophy (**D**) or eGFP expression (**E**) by 24h. Errorbars indicate median and interquartile range *** p<2*10^-16 *vs*. DMSO control, Kruskal–Wallis H test followed by one-sided Mann–Whitney U post-hoc test with Benjamini-Hochberg multiple testing correction, n = 2062-3416 cells.

(**F**) eCDFs of distributions of cell areas (same data as in **D**).

(**G**) Percent of cells with areas greater than DMSO 75th percentile at 24h (same data as in (**D**). *** p ≤ 1.58*10^−6, mixed−effects ANOVA followed by Tukey HSD, n = 2 independent cell isolations.

(**H**) 48h cell morphology metrics of cells treated with either 50 μM PE or 0.1% DMSO vehicle control. Solid lines indicate population median, errorbars indicate interquartile range. p-values represent Kruskal–Wallis H test followed by one-sided Mann–Whitney U post-hoc test with Benjamini-Hochberg multiple testing correction.

(**I**) Single-cell dynamics of cellular or nuclear metrics in response to either 50 μM PE or 0.1% DMSO control. Solid lines indicate population median, shaded areas indicate interquartile range.

Isoproterenol induces biphasic dose-dependent hypertrophy and apoptosis dynamics

In silico reconstructions of the *in vitro* cardiomyocyte hypertrophy signaling network have identified the βA signaling pathway as one that is potentially both hypertrophic and apoptotic (Kang et al., 2015; Ryall et al., 2012). The catecholamine isoproterenol (ISO) is a non-specific β-adrenergic receptor agonist and has been separately characterized as being either hypertrophic or apoptotic (Bass et al., 2012; Ryall et al., 2014; Yang et al., 2013; Zaugg et al., 2000). Our assay provides a unique opportunity to investigate dynamic single-cell decision-making between these two co-regulated phenotypes (Putinski et al., 2013; van Empel and De Windt, 2004).

To our knowledge, our assay shows for the first time that treatment with high concentration of ISO induces both hypertrophy and apoptosis in the same cell population (**Figure 4A**). ISO was

275 previously shown to regulate cardiomyocyte contractility and hypertrophy with distinct
276 concentration-dependence (Yang et al., 2013, p. 201). Therefore we examined the concentration-
277 dependence of ISO-induced hypertrophy and apoptosis. Interestingly, ISO induced a biphasic
278 concentration-dependent hypertrophy response, with diverging population-level hypertrophy
279 responses after 24 hours (**Figure 4B** and **C**). While all ISO-treated conditions induced some
280 level of hypertrophy relative to the DMSO vehicle-treated control within 24 hours of treatment,
281 medium to high doses of isoproterenol (10 to 100 μM ISO) induced less hypertrophy or
282 plateaued compared to lower doses. This plateau was especially striking after 24 hours (**Figure**
283 **4D**), the timepoint associated with apoptotic responses for STS stimuli. In contrast to the
284 biphasic hypertrophy response, A5 binding showed an ultrasensitive response with enhanced
285 apoptosis only at very high ISO concentrations (**Figure 4A**, **E**, and **F**). As commitment to
286 apoptosis is a binary decision (Roux et al., 2015), we analyzed single-cell trajectories which
287 indicated substantial variability in the response to 100 μM ISO (**Figure 4G**). Moreover,
288 apoptotic cells were smaller at time of A5 binding than their surviving counterparts (**Figure**
289 **4H**), further suggesting a relationship between growth and death phenotypes.

290 Like ISO, stimulation with a second adrenergic catecholamine, norepinephrine, also elicited
291 biphasic hypertrophic eGFP expression and ultrasensitive apoptosis (**Supplemental Figure**
292 **3**). However the apoptosis due to ISO or norepinephrine was not blocked by β-adrenergic
293 antagonist propranolol (Black et al., 1964) (**Supplemental Figure 4**), suggesting incomplete
294 inhibition or non-β-adrenergic mechanisms for apoptosis. This effect was replicated with
295 combination treatment with ISO, ICI-118,551 (selective β2 antagonist), and CGP 20712
296 (selective β1 antagonist) as well as combination treatment with ISO and Rp-cAMPs (selective
297 inhibitor of PKA) (**Supplemental Figure 5**).

298 CaMKII signaling has been shown previously to contribute to cardiomyocyte hypertrophy or
299 apoptosis under various models of cardiac injury (Vila-Petroff et al., 2007, p.; Zhu et al., 2003).

Therefore we asked whether CaMKII inhibition would modulate single-cell decisions of hypertrophy and apoptosis. Combination treatment with ISO and KN-93, a CaMKII inhibitor, increased apoptosis relative to combination treatment with ISO and KN-92, an inactive analogue of KN-93 (**Supplemental Figure 6**).

As a previous study showed that sub-apoptotic levels of caspase-3 were surprisingly required for hypertrophy(Putinski et al., 2013), we tested the caspase-3 inhibitor Z-DEVD-FMK in our system. The addition of Z-DEVD-FMK increased the proportion of grower cells while decreasing the proportion of shrinker cells, in contrast to previous reports (Putinski et al., 2013) (**Supplemental Figure 7A**). This effect was potentially mediated by the decrease in cardiomyocyte apoptosis. (**Supplemental Figure 7B and C**).

Previous studies have shown that catecholamine oxidation may contribute to cellular responses both in vitro and in vivo (Remião et al., 2002) . We tested whether preventing ISO oxidation with ascorbic acid would modulate ISO-induced apoptosis, but it did not (**Supplemental Figure 8**). Therefore it is unlikely that the ISO-induced apoptosis is due to oxidative byproducts.

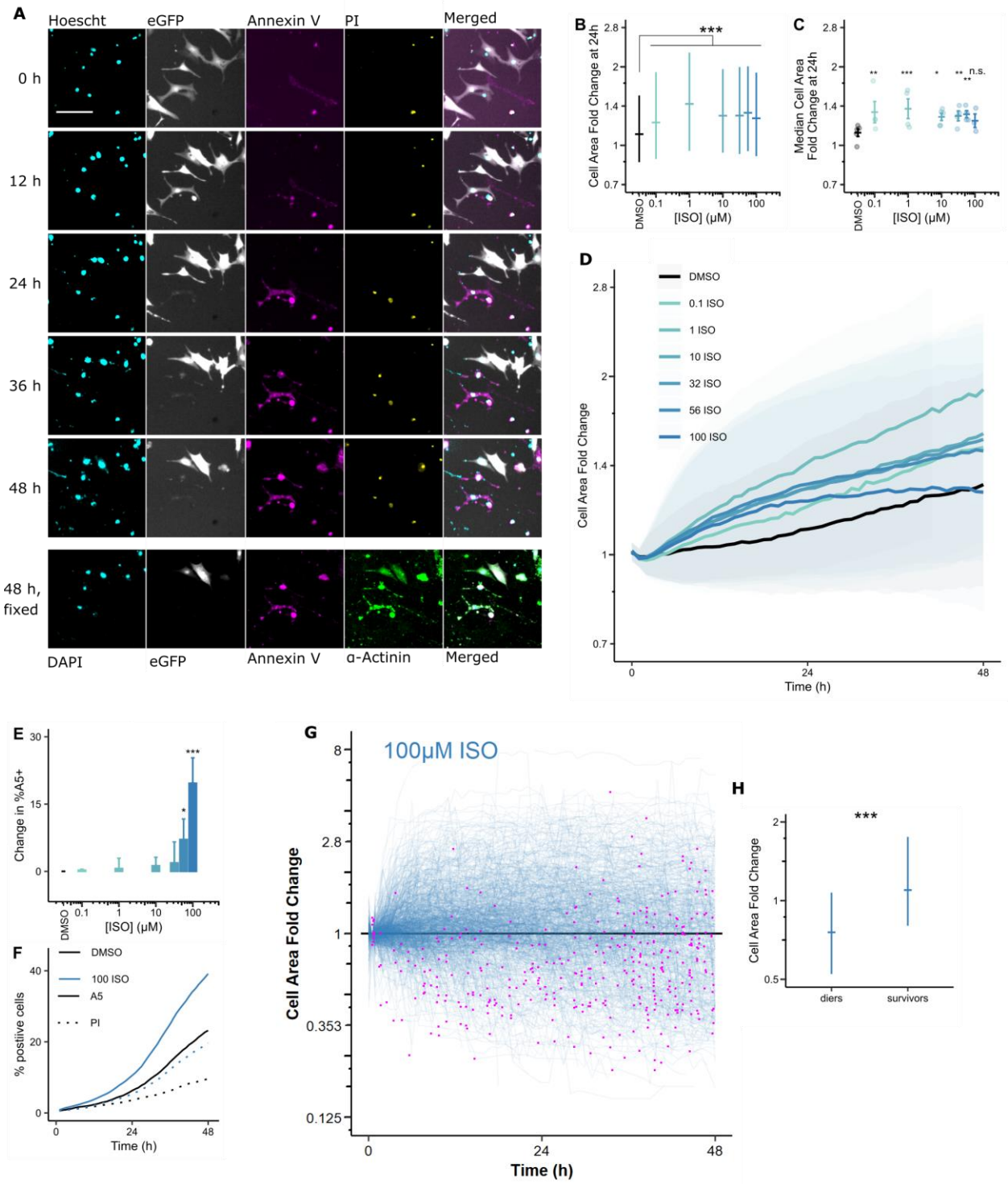

Figure 4. Single-cell dynamics of cardiomyocyte hypertrophy and apoptosis in response to isoproterenol.

(**A**) Representative timelapse images of neonatal rat cardiac cells treated with 100 μM ISO showing induction of hypertrophy and A5 binding (magenta).

(**B**) Single-cell ISO concentration hypertrophy responses at 24 h. Solid lines indicate population median, errorbars indicate interquartile range. ***all ISO-treated conditions were significant

with $p \leq 2.8*10^{-20}$ *vs.* DMSO control; Kruskal–Wallis H test followed by one-sided Mann–Whitney U post-hoc test with Benjamini-Hochberg multiple testing correction, n = 4067-6780 cells.
(**C**) Median ISO concentration hypertrophy responses at 24 h across experiments. Errorbars represent standard error of the mean. * p<0.05, **p<0.01, ***p<0,001; mixed effects ANOVA followed by one-sided Dunnett post hoc test, n=3-5 independent cell isolations.
(**D**) 48h ISO concentration response of hypertrophy dynamics. Shaded area represents interquartile range.
(**E**) ISO concentration A5 binding response across 48 h. *p = 0.055, *** p=7.53*10^-8 vs DMSO control; mixed effects ANOVA followed by Dunnett post hoc test, same n = 3-5 independent cell isolations as in (C).
(**F**) Empirical cumulative distribution function of A5 (magenta) and PI (yellow) binding for all cells treated either with DMSO or 100 μM ISO.
(**G**) Representative single-cardiomyocyte dynamic traces of morphology of cells treated with 100 μM ISO. Magenta dots indicate onset of A5 binding.
(**H**) Hypertrophy response of either area fold change at time of A5 binding (diers) or end of timecourse (survivors). Solid lines indicate population median, errorbars indicate interquartile range. *** p<2.2*10^-16 *vs.* DMSO control, one-sided Mann-Whitney U test, n = 3268-5081 cells.

Differential response of cardiomyocyte subpopulations contribute to biphasic hypertrophy and ultrasensitive apoptosis

We hypothesized that the biphasic population-level responses to ISO may reflect heterogeneity in single-cell decision making between cell growth and death, with potential for functional crosstalk between these cell responses encompassed by three possible conceptual models (**Figure 5A**). To facilitate comparison of cell hypertrophy and apoptosis, we first classified cells as “growers” , “stunned” , or “shrinkers”. Strikingly, the hypertrophic dynamics of these three subpopulations (**Figure 5B**) are qualitatively distinct from the transient population-level hypertrophic to 100 μM ISO (**Figure 4B**). Thus, the transient population-level hypertrophy results from the early increases in cell area of the “growers,” followed by the later decreased cell area of the “shrinkers,” and some cells remaining “stunned”. The “shrinker” subpopulation was more prone to cell death and therefore contributed to the decrease in median cell population area observed at later timepoints and higher ISO doses (**Figure 4E** and **H**).

356 As expected from the single-cell ISO concentration hypertrophy responses at 24 h, we saw a
357 trend towards an increased proportion of grower cells with ISO stimulation compared to DMSO.
358 In addition, the largest proportion of grower cells was seen with 1 μM ISO, which corresponds to
359 the dose at which we saw the greatest population-level hypertrophy response (**Figures 5C** and
360 **4C**,**D**). The relative decrease in proportion of grower cells as ISO concentration is increased
361 beyond 10 μM also correlated with the plateauing of the population-level hypertrophy ISO
362 concentration response (**Figure 4C** and **D**).

363 We hypothesized that growth and death responses may be related at the single cell level, with
364 apoptosis primarily occurring in "shrinker" cells. We quantified the proportions of cells from the
365 three growth subpopulations that contribute to the ultrasensitive response of A5 binding with
366 increasing ISO concentration (**Figure 5D**). At 100 μM ISO, shrinkers and stunned cells were
367 indeed statistically more likely than growers to become A5 positive, leading us to favor a "grow-
368 or-die" model over the "grow-and-die" model. However, in contrast to our hypothesis, the
369 quantitative contributions to death responses were fairly similar (**Figure 5E**). These
370 concentration-dependent hypertrophy and apoptosis decisions are summarised in **Figure 5F**.

371 Having found that apoptotic cells also tended to become smaller (**Figure 4H**), we further
372 analyzed the growth and death kinetics of the hypertrophic subpopulations to determine
373 additional causes for the biphasic hypertrophy concentration response observed at the
374 population level. We measured the time at which each cell achieved maximal cell area.
375 Furthermore, if the cell became A5 positive, we measured the time lag between those two events
376 (**Figure 5G**). We found that the hypertrophic subpopulations differed not only in the
377 magnitude of their hypertrophy, but also the time at which they achieved their maximal
378 hypertrophy. Stunned cells grew to their maximal extent before 24 hours while growers
379 continued growing after 24 hours. As expected, shrinkers had maximal area at the start of the
380 time course (**Figure 5H**). Even though the three hypertrophic subpopulations differed

381 significantly in their hypertrophic kinetics, the dead cells in the grower and stunned populations
382 bound A5 with statistically different yet fairly similar delay after their maximal cell area.
383 However, the shrinker cells showed a striking difference from other subpopulations, with a
384 bimodal distribution in delay from maximal cell area to A5 binding. Indeed, almost half of the
385 shrinker cells persisted at least 24 hours before binding A5 (**Figure 5I**). From this analysis, we
386 identified that the source of the biphasic cell population hypertrophy ISO concentration
387 response was a subpopulation of cells that underwent cell shrinkage and then delayed apoptosis,
388 while cell hypertrophy may represent a protective mechanism against apoptosis. The presence of
389 these distinct subpopulation behavior may represent an incoherent feedforward network motif
390 between βA stimulation, hypertrophy, and apoptosis.

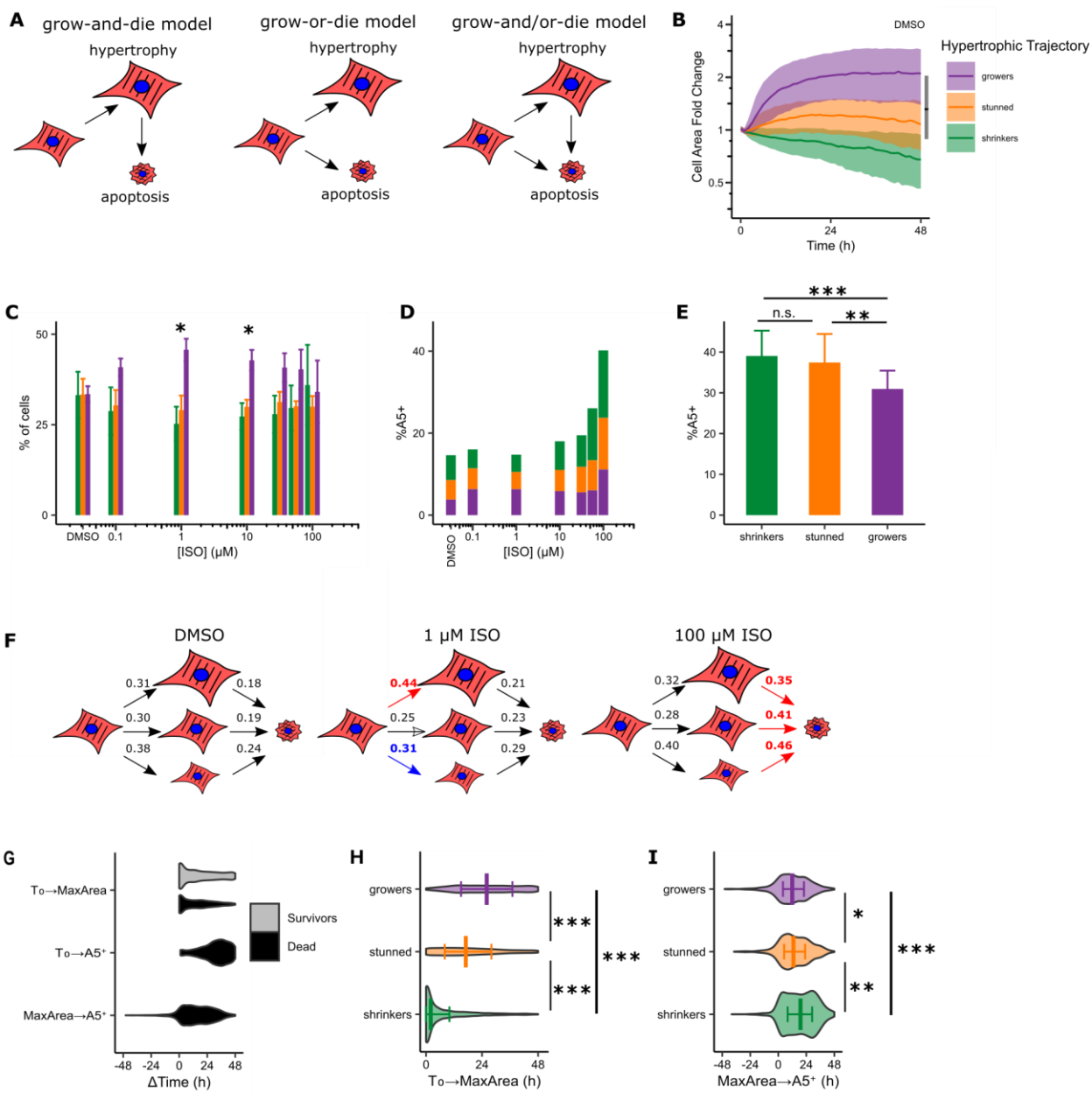

Figure 5. Single-cell hypertrophy-apoptosis decision making in cardiomyocytes treated with 100 μM ISO.

All data is the same as in Figure 4.

(**A**) Schematic of possible cardiomyocyte phenotypic decision-making models and relationships between hypertrophy and apoptosis.

(**B**) The population of cells treated with 100 μM ISO was partitioned into 3 hypertrophic trajectory groups relative to DMSO-treated population at 48 h. Growers (purple) were defined as cells whose max fold change area was greater than that of the 75th percentile of the DMSO-treated population. Stunned (orange) cells were defined as cells whose max fold change area was in the DMSO-treated interquartile range. Shrinkers (green) were defined as cells whose max fold change area was less than the 25th percentile of the DMSO-treated cells. Solid lines indicate

population median, shaded areas indicate interquartile range, black line indicates population median

(**C**) Concentration response of cell population makeup. Errorbars represent mean ± SEM. Comparisons were made between each treatment's percent "grower" subpopulation; while the overall mixed-effects ANOVA was not statistically significant (p=0.094) the more powered one-sided Dunnett's test showed statistically significant differences indicated with * p<0.05 vs DMSO control, n = 3-4 biological replications. Moreover, the mixed-effects ANOVA between the 3 hypertrophy subpopulations was not significant for the DMSO-treatment. However, there was a significant increase in the proportion of the grower subpopulation relative to the other two subpopulations with p<0.01, mixed-effects ANOVA followed by Tukey HSD.

(**D**) Concentration response of cell population makeup for all apoptotic cells (same data as **Figure 4F**).

(**E**) Cell population makeup. Errorbars represent mean ± SEM. ** p = 0.00562, ***p<0.001, mixed-effects ANOVA followed by Tukey HSD, n = 3 independent cell isolations.

(**F**) Hypertrophy and apoptosis transition state diagrams for different ISO concentrations.

(**G**) Single-cell quantification of onset of maximal hypertrophic area and A5 binding and with the lag between those two events.

Time to maximal hypertrophy (**H**, n = 2378-3375 cells) or time between maximal hypertrophy and A5 binding (**I,** n = 824-1440) for each hypertrophic trajectory group from **G**. Solid lines indicate population median, errorbars indicate interquartile range.*p=0.017, **p=9.0*10^-14, *** p<2*10^-22, Kruskal–Wallis H test followed by Dunn's All-Pairs Rank Comparison post-hoc test with Benjamini-Hochberg multiple testing correction.

Initial cell morphology and nucleus predicts cellular decision-making

Given the considerable single-cell heterogeneity in response to ISO stimulation, we asked whether pre-existing features of cardiomyocytes would predict their subsequent growth and death. We used a multinomial log-linear regression model to identify cellular features that predict hypertrophy-apoptosis decision-making (**Methods, Figure 6A, Supplemental Table 1**). The response variable was one of 6 pairwise combinations of the 3 hypertrophic trajectory classifications and the binary survival/death outcome. The predictor variables were the 6 cellular and 6 nuclear size, shape and fluorescence intensity metrics identified by our assay as potentially relevant to cardiomyocyte apoptosis and hypertrophy (**Figures 2** and **3**). 5-fold cross validation repeated 100 times showed that the model predicts the single-cell hypertrophy-apoptosis response to 100 μM ISO with an accuracy of 32.2±0.1% (mean±SEM) and $R^2_{McFadden}$ of 0.075. This accuracy was similar to that of a random forest model approach (accuracy of

439 32.7±0.1%, mean±SEM, **Supplemental Figure 9B**) but the multinomial regression model
440 approach provides value in the interpretability of the coefficient values of each classifier. Both
441 models performed significantly better than the multinomial null model (accuracy of 20.8±0.01,
442 mean±SEM). Similarity of accuracy in both approaches suggests that differences in model
443 structure were less important than unmeasured initial features or sources of stochasticity.

444 Analysis of the log-linear model identified several initial cell metrics that were predictive of
445 hypertrophy, apoptosis, or both. One such metric was the initial cell area - the model predicted
446 that initially larger cells had higher likelihoods of being stunned or shrinking and a lower
447 likelihood of growing. The relationships identified in the model between initial cell features and
448 growth-death responses motivated further verification. Indeed, growers had an initial cell size
449 that was smaller than shrinker or stunned subpopulations (**Figure 6B**). Analysis of the growth
450 trajectory of cells in either the bottom or top quartiles of initial cell area distributions also
451 showed that small cells had a hypertrophic growth response while larger cells did not
452 hypertrophy significantly (**Figure 6C**). While the initial area regression coefficient did not
453 specifically correlate with the survival status of a cell, it had an especially strong statistical
454 association with the shrinker/dier population. Indeed, cells in the largest quartile of initial cell
455 areas were more likely to die than those in the smallest quartile (**Figure 6D**). A parallel random
456 forest regression model showed that the initial area was the most influential metric for model
457 accuracy (**Supplemental Figure 9C**). These initial cell size-dependent hypertrophy and
458 apoptosis decisions are summarised in **Figure 6F**. Our data suggest that while hypertrophic
459 signaling confers partial protection against apoptosis, ISO stimulation still generates a
460 population of hypertrophic cells that go on to die. Thus, our data best supports the "grow-
461 and/or-die" model over the "grow-or-die" model.

462 Interestingly, this analysis identified nuclear Hoechst intensity and its median absolute
463 deviation as two nuclear metrics associated with both cell growth and survival (**Figure 6A**). The

464 median absolute deviation metric was also implicated as the second most influential metric for
465 model accuracy by the random forest model (**Supplemental Figure 9C**). Similarly, our single-
466 cell analysis show that cells of the grower-survivor subpopulation initially have less compacted
467 chromatin compared to cells in all other subpopulations, which we also observed in our PE- and
468 56 μM ISO treated cells at the population level (**Figure 6E** and **3I** and **Supplemental Figure**
469 **1**).

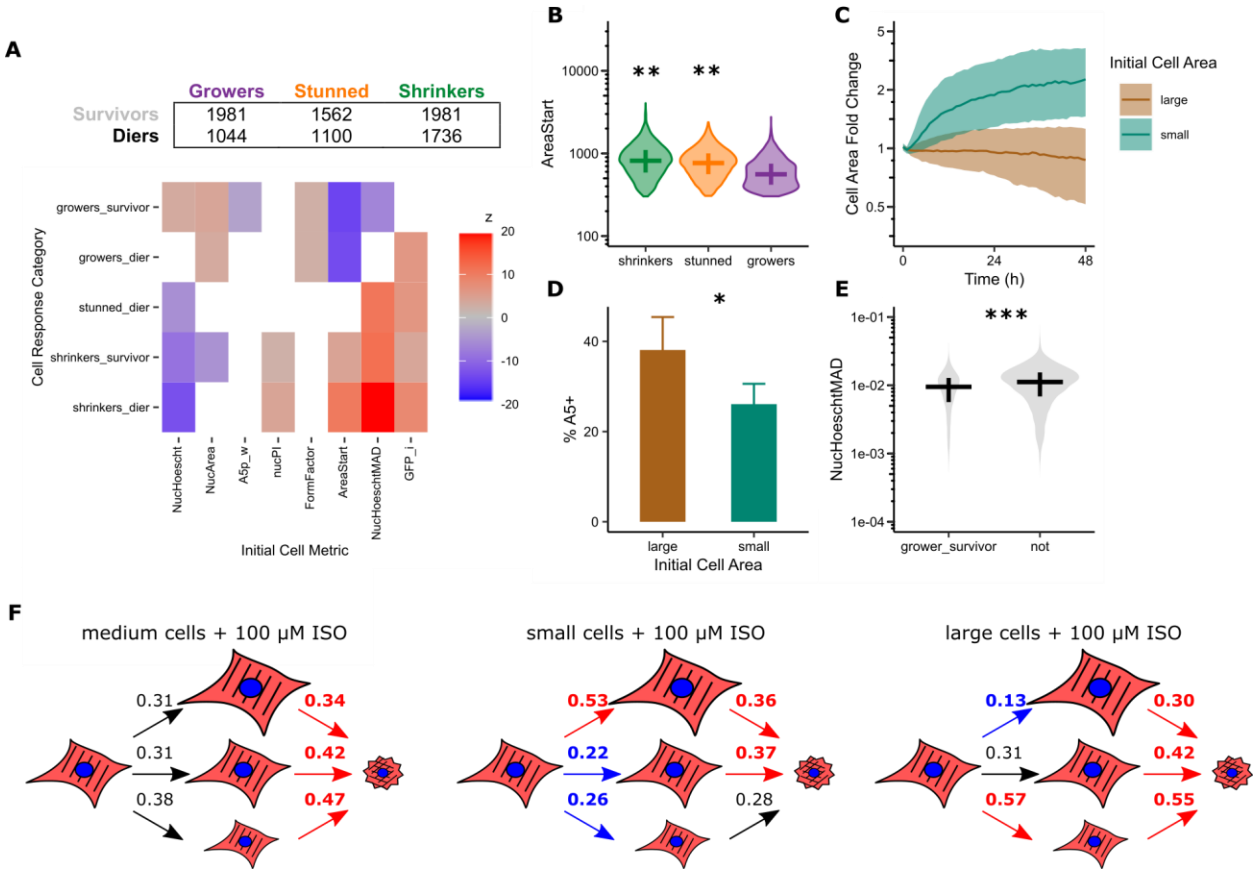

Figure 6. Multinomial log-linear model reveals predictors of single-cell hypertrophy-apoptosis decision making in cardiomyocytes treated with 100 μM ISO.

All data is the same as in Figure 4.

(**A**) Significant multinomial log-linear model coefficient z-scores. The contingency table contains the number of cells in each hypertrophy-death category. The model self-validates with an accuracy of 33.26% ($R^2_{McFadden}$ = 0.075), with a 5-fold cross-validation accuracy of 32.33+/-0.01% (n=100 permutations) (**Supplemental Figure 9)**.

(**B**) Initial cell areas of each hypertrophic trajectory group. Solid lines indicate population median, error bars indicate interquartile range. ** $p \leq 2*10^{-16}$ *vs.* grower population, Kruskal–Wallis H test followed by one-sided Mann–Whitney U post-hoc test with Benjamini-Hochberg multiple testing correction, n = 2662-3738 cells.

(**C**) 48h hypertrophy dynamics of cells in either the bottom or top quartile of initial cell area. Solid lines indicate population median, shaded areas indicate interquartile range.

(D) 48h total A5 binding of cells in either the bottom or top quartile of initial cell area. * p= 0.027, one-sided Welch's paired T-test, n = 3 independent cell isolations.

(E) Initial nuclear Hoechst MAD of grower-survivor group vs. all other cells. Solid lines indicate population median, errorbars indicate interquartile range. *** p = 2.4*10^-36, one-sided Mann-Whitney U test, n = 1981-7444 cells.

(F) Hypertrophy and apoptosis transition state diagrams for different cardiomyocyte subpopulations. Arrow colors are relative to the DMSO diagram in **Figure 5F**.

Discussion

Single-cell, multiplexed, or longitudinal data each have potential for elucidating new causal relationships or differential cell responses to stimuli (Boutros et al., 2015; Sugihara et al., 2012; Vilela and Danuser, 2011). Expression of the fetal gene program is a common surrogate for cardiomyocyte hypertrophy measurements (Bilsen and Chien, 1993; Tsai et al., 2017), but bulk measurements capture neither the changes in cell morphology nor nuances of single-cell behaviors. Fixed cell cytometry approaches may capture phenotypic endpoints but lack information about initial system state or the phenotypic trajectories necessary to elucidate decision-making processes without the use of additional system perturbations (Heijink et al., 2019; Putinski et al., 2013; Vilela and Danuser, 2011). Previous studies of single-cell decision-making have largely been in non-myocytes and have examined decision-making for a single phenotype(Fallahi-Sichani et al., 2017; Paek et al., 2016; Roux et al., 2015). Here, our high-content imaging study extends previous work on automated live imaging of single-cell hypertrophy to address challenges of measuring single-cell hypertrophy and apoptosis simultaneously. This study leveraged simple genetically encoded and biochemical fluorescent reporters to track morphological and biochemical dynamics in single cells necessary to investigate fundamental cell decisions of growth and death.

After validating our cardiomyocyte assay for hypertrophy and apoptosis measurements separately and identifying new features of those processes, we used our assay to examine the dynamics of decision-making between hypertrophy and apoptosis in response to catecholamines. Theoretical mechanisms underlying simultaneous regulation of analog and digital phenotypic decision-making by a single signaling network have been proposed. To our knowledge, however, the relative timing of early analog hypertrophy responses and late digital apoptosis decisions represents the first experimental support of a single signaling network

516 regulating a mixture of analog and digital phenotypic decisions (Kovary et al., 2018).
517 Leveraging these heterogeneity dynamics in our cell populations, we identified a biphasic
518 hypertrophic ISO concentration response at the cell-population level, suggesting at least two
519 underlying, competing processes. We therefore hypothesized that different subpopulations of
520 cells contribute to the overall population response.

521 Our data best supports the "grow-and/or-die" conceptual model in which hypertrophic signaling
522 is moderately protective against apoptosis. Low- to mid-concentrations of ISO increased the
523 proportion of cells that hypertrophied and resisted apoptosis, while high ISO concentrations
524 increased the number of cells susceptible to death. We used cyclic data-driven hypothesis testing
525 and modelling to identify characteristic features of these different subpopulations. Our
526 multinomial log-linear regression models sought to identify nongenetic heterogeneities in initial
527 cell size, morphology, and fluorescence metrics at a single ISO dose that would predict dynamic,
528 single-cell decision-making. This modeling approach had an accuracy rate similar to the more
529 agnostic, black-box random forest model. This suggests that differences in model structure
530 (such as the presence of non-linear interactions between predictors) were less important than
531 other, non-characterized factors or biochemical sources of stochasticity that our high-content
532 imaging assay did not capture (Hilfinger and Paulsson, 2011; Swain et al., 2002). Even so, we
533 identified and validated the initial cell size as a predictor of hypertrophic trajectory and
534 susceptibility to death. Surprisingly, we identified two nuclear metrics, DNA content and
535 chromatin homogeneity, that predicted cell hypertrophy and survival, which suggest a potential
536 role for transcriptional regulation of differential cell decision-making (Liu and Tang, 2019;
537 Symmons and Raj, 2016). These three metrics were also predictive of hypertrophy/apoptosis
538 decision-making with other treatments, namely PE and other ISO concentrations.

539 We envision multiple avenues for extending the approach presented herein. Tracking *in vitro*
540 co-culture models of cardiomyocytes and fibroblasts and the relative local density of those cells

541 would provide new insight into paracrine signaling interactions between cardiomyocytes and
542 fibroblasts to yield new potential therapeutic targets (Piek et al., 2016). We have also previously
543 described a screen for cardiomyocyte proliferation using methods compatible with those
544 presented here, suggesting a potential third phenotype to be multiplexed with our assay (Woo et
545 al., 2019). Our fluorescent reporter could be replaced with reporters of signaling pathway
546 activity to provide mechanistic insight into cellular decision-making (Gross et al., 2019). Finally,
547 techniques such as cyclic immunofluorescence (Lin et al., 2015) may be incorporated to provide
548 additional mechanistic insight into the question of whether form follows function, or function
549 follows form in the context of heart failure and as suggested by our results. High-content live-
550 cell imaging as presented here can thus improve understanding of cellular multi-tasking in
551 response to stress.

552 Materials and Methods

553 ***Chemical Reagents***

554 - DMSO (R&D Systems, Cat#3176)
555 - Staurosporine (R&D Systems, Cat#1285)
556 - (R)-(-)-Phenylephrine hydrochloride (R&D Systems, Cat#2838)
557 - Isoproterenol hydrochloride (R&D systems, Cat#1747)
558 - L-ascorbic acid (R&D Systems, Cat#4055)
559 - (-)-Norepinephrine (Sigma-Aldrich, Cat#A7257)
560 - Propranolol hydrochloride (R&D Systems, Cat#0624)
561 - ICI-118,551 (R&D Systems, Cat#0821)

562 - CGP-20712 (R&D Systems, Cat#1024)

563 - KN-92 (R&D Systems, Cat#4130)

564 - KN-93 (R&D Systems, Cat#1278)

565 - Z-DEVD-FMK (R&D Systems, Cat#2166)

566 ***Lentivirus***

567 Lentiviruses were prepared in 293T/17 cells (ATCC) by triple transfection with psPAX2,
568 pMD.2G, and PLX302 eGFP as previously described (Bajikar et al., 2017; Wang et al., 2011). The
569 plasmids were a gift from K. Janes (University of Virginia).

570 ***Cell Culture***

571 Cardiac myocytes were harvested from 1–2 day-old Sprague-Dawley rats using the Neomyts
572 isolation kit (Cellutron, Baltimore, MD). All procedures were performed in accordance with the
573 Guide for the Care and Use of Laboratory Animals published by the U.S. National Institutes of
574 Health and approved by the University of Virginia Institutional Animal Care and Use
575 Committee. Myocytes were cultured in plating media (Dulbecco's modified Eagle media
576 supplemented with 17% M199, 10% horse serum(Gibco, 16050122), 5% fetal bovine serum
577 (HyClone FBS Thermo Scientific Cat: SH30396.03 Lot: AUD34652), 50 U/mL penicillin, 50
578 µg/mL streptomycin (Gibco, 15140122), 4.8mM L-glutamine(Gibco, 25030081) at a density of
579 20,000 cells per well of a 96-well CellBIND plate (Corning) coated with SureCoat (Cellutron).
580 Cells were transduced with 100µL of eGFP lentivirus and plating media supplemented with
581 8µg/mL polybrene (Santa Cruz Biotechnology, Cat#sc-134220) at the time of plating and after
582 24 hours. 36 hours after plating, the medium was replaced with low-serum media (phenol-red
583 free Dulbecco's modified Eagle media supplemented with 17% M199, 0.1% FBS, 1% ITSS, 20mM

584 HEPES, 50 U/mL penicillin, 50 μg/mL streptomycin, 4.8mM L-glutamine) for 24 hours of
585 serum starvation prior to treatment.

586 ***Dual hypertrophy/apoptosis assay***

587 Cells were pre-stained and pre-treated with relevant small molecule inhibitors in low-serum
588 media supplemented with 27nM Hoechst 33342, 0.5nM Propidium iodide, and 0.5× Alexa Fluor
589 647–conjugated A5 (Invitrogen) for 2 hours. Cells were imaged on the Operetta CLS high-
590 content imaging system (Perkin-Elmer) using a 10 × 0.3NA objective and the temperature and
591 CO2 control option set to 37°C and 5% CO2, respectively. Images were captured every 1 hour for
592 48 hours. 4 fields of view were acquired for each well.

593 After live-cell imaging, the cells were fixed with 4% PFA and stained with DAPI and monoclonal
594 anti-α-Actinin antibody (Sigma, Cat#A7811). The same fields of view acquired during live
595 imaging were again imaged.

596 ***Image Processing***

597 All images were processed using Matlab 2018a (MathWorks), ilastik(Berg et al., 2019), and
598 CellProfiler(Kamentsky et al., 2011). Images were flat-field corrected in Matlab using reference
599 dark field and flat-field images taken of fluorescence reference slides (Ted Pella). Corrected
600 fluorescence signals from GFP, A5, and α-Actinin images were converted to probability maps
601 using the pixel classification tool in ilastik (Berg et al., 2019).

602 An image analysis pipeline was developed in CellProfiler to automatically segment, measure,
603 and classify the cells from the corrected images and signal probability maps. Briefly, all live
604 timepoints and fixed immunofluorescence images were aligned to the final timepoint images.
605 Hoechst- and propidium iodide-positive nuclei were independently segmented using Otsu
606 thresholding. Binucleates were identified by merging touching nuclei and then shrunken by a
607 radius of 1 pixel. GFP positive cells were identified using a watershed segmentation algorithm on

608 the GFP probability map using the merged nuclei as starting seeds. These GFP positive cells
609 were tracked and measured for morphological and fluorescence intensity characteristics
610 including area, GFP intensity, A5 intensity and probability, final α-Actinin intensity and
611 probability. Nuclei were also measured for morphological and propidium iodide and Hoechst
612 intensities.

613 ***Statistical Analysis***

614 All statistical analyses were done in R version 3.6.3 (R Core Team, 2020). The following
615 packages were additionally used for general data preparation and visualization: tidyverse
616 (Wickham et al., 2019), multcomp (Hothorn et al., 2008), nlme(Pinheiro et al., 2020), nnet
617 (Venables and Ripley, 2002), perturb (Hendrickx, 2019), PMCMRplus(Pohlert, 2020),
618 randomForest (Liaw and Wiener, 2002), stargazer (Hlavac, 2018) and tableplot (Kwan and
619 Friendly, 2012).

620 ***Modelling***

621 Data were normalized prior to statistical modelling. For multinomial log-linear modelling,
622 predictor variables were filtered for multicollinearity on the basis of their variance inflation
623 factor (VIF) scores - removal of the raw major axis length metric reduced all VIF scores below a
624 maximum of 2.4. We also verified the remaining collinearities with a tableplot and that those
625 variables described sufficiently different metrics (**Supplemental Figure 9A**). For random
626 forest modelling, default values from the randomForest package were used with the exception of
627 1000 trees (Liaw and Wiener, 2002).

Funding

This work was funded by the National Institutes of Health (BC: HL134266, GM007267, GM008715; JJS: HL13775, HL137100; OD021723) and National Science Foundation (1252854).

Acknowledgements

We thank members of the Saucerman lab, including B. Wissmann for technical support with cardiomyocyte isolations, P. Tan for support with CellProfiler, and L. Woo for discussions and providing feedback on this work. We also thank Chris Smolko and Kevin Janes for contributing the eGFP lentivirus. We acknowledge Research Computing at The University of Virginia for providing computational resources and technical support.

Author contributions

Conceptualization, B.C. and J.J.S.; Methodology, B.C. and J.J.S.; Investigation, B.C. and J.J.S.; Writing, B.C. and J.J.S.; Funding Acquisition, J.J.S.; Supervision, J.J.S..

References

Bajikar, S.S., Wang, C.-C., Borten, M.A., Pereira, E.J., Atkins, K.A., and Janes, K.A. (2017). Tumor Suppressor Inactivation of GDF11 Occurs by Precursor Sequestration in Triple-Negative Breast Cancer. Dev. Cell *43*, 418-435.e13.

Bass, G., Ryall, K., Katikapalli, A., Taylor, B., Dang, S., Acton, S., and Saucerman, J. (2012). Automated image analysis identifies signaling pathways regulating distinct signatures of cardiac myocyte hypertrophy. J. Mol. Cell. Cardiol. *52*, 923–930.

Behar, M., Dohlman, H.G., and Elston, T.C. (2007). Kinetic insulation as an effective mechanism for achieving pathway specificity in intracellular signaling networks. Proc. Natl. Acad. Sci. U. S. A. *104*, 16146–16151.

Behar, M., Barken, D., Werner, S.L., and Hoffmann, A. (2013). The Dynamics of Signaling as a Pharmacological Target. Cell *155*.

Belmokhtar, C.A., Hillion, J., and Ségal-Bendirdjian, E. (2001). Staurosporine induces apoptosis through both caspase-dependent and caspase-independent mechanisms. Oncogene *20*, 3354–3362.

Berg, S., Kutra, D., Kroeger, T., Straehle, C.N., Kausler, B.X., Haubold, C., Schiegg, M., Ales, J., Beier, T., Rudy, M., et al. (2019). ilastik: interactive machine learning for (bio)image analysis. Nat. Methods *16*, 1226–1232.

Bilsen, M. van, and Chien, K.R. (1993). Growth and hypertrophy of the heart: towards an understanding of cardiac specific and inducible gene expression. Cardiovasc. Res. *27*, 1140–1149.

Black, J.W., Crowther, A.F., Shanks, R.G., Smith, L.H., and Dornhorst, A.C. (1964). A NEW ADRENERGIC: BETA-RECEPTOR ANTAGONIST. The Lancet *283*, 1080–1081.

Boutros, M., Heigwer, F., and Laufer, C. (2015). Microscopy-Based High-Content Screening. Cell *163*, 1314–1325.

D'Angelo, D.D., Sakata, Y., Lorenz, J.N., Boivin, G.P., Walsh, R.A., Liggett, S.B., and Dorn, G.W. (1997). Transgenic Galphaq overexpression induces cardiac contractile failure in mice. Proc. Natl. Acad. Sci. U. S. A. *94*, 8121–8126.

van Empel, V.P.M., and De Windt, L.J. (2004). Myocyte hypertrophy and apoptosis: a balancing act. Cardiovasc. Res. *63*, 487–499.

Fallahi-Sichani, M., Becker, V., Izar, B., Baker, G.J., Lin, J., Boswell, S.A., Shah, P., Rotem, A., Garraway, L.A., and Sorger, P.K. (2017). Adaptive resistance of melanoma cells to RAF inhibition via reversible induction of a slowly dividing de-differentiated state. Mol. Syst. Biol. *13*.

Frey, N., Katus, H.A., Olson, E.N., and Hill, J.A. (2004). Hypertrophy of the heart: a new therapeutic target? Circulation *109*, 1580–1589.

Friendly, M., and Kwan, E. (2009). Where's Waldo? Visualizing Collinearity Diagnostics. Am. Stat. *63*, 56–65.

Greenwald, E., Redden, J., Dodge-Kafka, K., and Saucerman, J. (2013). Scaffold State-Switching Amplifies, Accelerates and Insulates PKC Signaling. J. Biol. Chem.

Grossman, W., Jones, D., and McLaurin, L. (1975). Wall stress and patterns of hypertrophy in the human left ventricle. J. Clin. Invest. *56*, 56–64.

Hayakawa, Y., Chandra, M., Miao, W., Shirani, J., Brown, J.H., Dorn, G.W., Armstrong, R.C., and Kitsis, R.N. (2003). Inhibition of cardiac myocyte apoptosis improves cardiac function and abolishes mortality in the peripartum cardiomyopathy of Galpha(q) transgenic mice. Circulation *108*, 3036–3041.

Hendrickx, J. (2019). perturb: Tools for Evaluating Collinearity.

Hlavac, M. (2018). stargazer: Well-Formatted Regression and Summary Statistics Tables.

Hothorn, T., Bretz, F., and Westfall, P. (2008). Simultaneous inference in general parametric models. Biom. J. Biom. Z. *50*, 346–363.

Imai, R., Nozaki, T., Tani, T., Kaizu, K., Hibino, K., Ide, S., Tamura, S., Takahashi, K., Shribak, M., and Maeshima, K. (2017). Density imaging of heterochromatin in live cells using orientation-independent-DIC microscopy. Mol. Biol. Cell *28*, 3349–3359.

Iwai-Kanai, E., Hasegawa, K., Araki, M., Kakita, T., Morimoto, T., and Sasayama, S. (1999). alpha- and beta-adrenergic pathways differentially regulate cell type-specific apoptosis in rat cardiac myocytes. Circulation *100*, 305–311.

Kamentsky, L., Jones, T.R., Fraser, A., Bray, M.-A., Logan, D.J., Madden, K.L., Ljosa, V., Rueden, C., Eliceiri, K.W., and Carpenter, A.E. (2011). Improved structure, function and compatibility for CellProfiler: modular high-throughput image analysis software. Bioinformatics *27*, 1179–1180.

Kang, J., Lee, H.-S., Kang, Y.-W., and Cho, K.-H. (2015). Systems biological approaches to the cardiac signaling network. Brief. Bioinform. bbv039.

Kovary, K.M., Taylor, B., Zhao, M.L., and Teruel, M.N. (2018). Expression variation and covariation impair analog and enable binary signaling control. Mol. Syst. Biol. *14*, e7997.
Kwan, E., and Friendly, M. (2012). tableplot: Represents tables as semi-graphic displays.
Lawrie, A.M., Noble, M.E., Tunnah, P., Brown, N.R., Johnson, L.N., and Endicott, J.A. (1997). Protein kinase inhibition by staurosporine revealed in details of the molecular interaction with CDK2. Nat. Struct. Biol. *4*, 796–801.
Levy, D., Garrison, R.J., Savage, D.D., Kannel, W.B., and Castelli, W.P. (1990). Prognostic Implications of Echocardiographically Determined Left Ventricular Mass in the Framingham Heart Study. N. Engl. J. Med. *322*, 1561–1566.
Liaw, A., and Wiener, M. (2002). Classification and Regression by randomForest. R News *2*, 18–22.
Lin, J.-R., Fallahi-Sichani, M., and Sorger, P. (2015). Highly multiplexed imaging of single cells using a high-throughput cyclic immunofluorescence method. Nat. Commun. *6*, 8390.
Liu, C.-F., and Tang, W.H.W. (2019). Epigenetics in Cardiac Hypertrophy and Heart Failure. JACC Basic Transl. Sci. *4*, 976–993.
Liu, Z., Yue, S., Chen, X., Kubin, T., and Braun, T. (2010). Regulation of Cardiomyocyte Polyploidy and Multinucleation by CyclinG1. Circ. Res. *106*, 1498–1506.
Meggio, F., Donella Deana, A., Ruzzene, M., Brunati, A.M., Cesaro, L., Guerra, B., Meyer, T., Mett, H., Fabbro, D., and Furet, P. (1995). Different susceptibility of protein kinases to staurosporine inhibition. Kinetic studies and molecular bases for the resistance of protein kinase CK2. Eur. J. Biochem. *234*, 317–322.
Morisco, C., Zebrowski, D.C., Vatner, D.E., Vatner, S.F., and Sadoshima, J. (2001). Beta-adrenergic cardiac hypertrophy is mediated primarily by the beta(1)-subtype in the rat heart. J. Mol. Cell. Cardiol. *33*, 561–573.
Nüsslein-Volhard, C., and Wieschaus, E. (1980). Mutations affecting segment number and polarity in Drosophila. Nature *287*, 795–801.
O'Connell, T.D., Ishizaka, S., Nakamura, A., Swigart, P.M., Rodrigo, M.C., Simpson, G.L., Cotecchia, S., Rokosh, D.G., Grossman, W., Foster, E., et al. (2003). The α1A/C- and α1B-adrenergic receptors are required for physiological cardiac hypertrophy in the double-knockout mouse. J. Clin. Invest. *111*, 1783–1791.
O'Connell, T.D., Jensen, B.C., Baker, A.J., and Simpson, P.C. (2014). Cardiac alpha1-adrenergic receptors: novel aspects of expression, signaling mechanisms, physiologic function, and clinical importance. Pharmacol. Rev. *66*, 308–333.
Ormerod, M.G., Sun, X.M., Snowden, R.T., Davies, R., Fearnhead, H., and Cohen, G.M. (1993). Increased membrane permeability of apoptotic thymocytes: a flow cytometric study. Cytometry *14*, 595–602.
Paek, A.L., Liu, J.C., Loewer, A., Forrester, W.C., and Lahav, G. (2016). Cell-to-Cell Variation in p53 Dynamics Leads to Fractional Killing. Cell *165*, 631–642.
Petkova, M.D., Tkačik, G., Bialek, W., Wieschaus, E.F., and Gregor, T. (2019). Optimal Decoding of Cellular Identities in a Genetic Network. Cell *176*, 844-855.e15.
Piek, A., de Boer, R.A., and Silljé, H.H.W. (2016). The fibrosis-cell death axis in heart failure. Heart Fail. Rev. *21*, 199–211.
Pinheiro, J., Bates, D., DebRoy, S., Sarkar, D., and R Core Team (2020). nlme: Linear and Nonlinear Mixed Effects Models.
Pohlert, T. (2020). PMCMRplus: Calculate Pairwise Multiple Comparisons of Mean Rank Sums Extended.
Putinski, C., Abdul-Ghani, M., Stiles, R., Brunette, S., Dick, S., Fernando, P., and Megeney, L. (2013). Intrinsic-mediated caspase activation is essential for cardiomyocyte hypertrophy. Proc. Natl. Acad. Sci. U. S. A. *110*, E4079–E4087.
R Core Team (2020). R: The R Project for Statistical Computing.
Remião, F., Carvalho, M., Carmo, H., Carvalho, F., and Bastos, M.L. (2002). Cu2+-induced isoproterenol oxidation into isoprenochrome in adult rat calcium-tolerant cardiomyocytes.

Chem. Res. Toxicol. *15*, 861–869.
Roux, J., Hafner, M., Bandara, S., Sims, J.J., Hudson, H., Chai, D., and Sorger, P.K. (2015). Fractional killing arises from cell-to-cell variability in overcoming a caspase activity threshold. Mol. Syst. Biol. *11*, 803.
Ryall, K.A., and Saucerman, J.J. (2012). Automated imaging reveals a concentration dependent delay in reversibility of cardiac myocyte hypertrophy. J. Mol. Cell. Cardiol. *53*, 282–290.
Ryall, K., Holland, D., Delaney, K., Kraeutler, M., Parker, A., and Saucerman, J. (2012). Network reconstruction and systems analysis of cardiac myocyte hypertrophy signaling. J. Biol. Chem. *287*, 42259–42268.
Ryall, K.A., Bezzerides, V.J., Rosenzweig, A., and Saucerman, J.J. (2014). Phenotypic screen quantifying differential regulation of cardiac myocyte hypertrophy identifies CITED4 regulation of myocyte elongation. J. Mol. Cell. Cardiol. *72*, 74–84.
Saito, S., Hiroi, Y., Zou, Y., Aikawa, R., Toko, H., Shibasaki, F., Yazaki, Y., Nagai, R., and Komuro, I. (2000). β-Adrenergic Pathway Induces Apoptosis through Calcineurin Activation in Cardiac Myocytes. J. Biol. Chem. *275*, 34528–34533.
Saucerman, J., and McCulloch, A. (2006). Cardiac beta-adrenergic signaling: from subcellular microdomains to heart failure. Ann. N. Y. Acad. Sci. *1080*, 348–361.
Sawyer, D.B., Siwik, D.A., Xiao, L., Pimentel, D.R., Singh, K., and Colucci, W.S. (2002). Role of oxidative stress in myocardial hypertrophy and failure. J. Mol. Cell. Cardiol. *34*, 379–388.
Schneider-Poetsch, T., Ju, J., Eyler, D.E., Dang, Y., Bhat, S., Merrick, W.C., Green, R., Shen, B., and Liu, J.O. (2010). Inhibition of Eukaryotic Translation Elongation by Cycloheximide and Lactimidomycin. Nat. Chem. Biol. *6*, 209–217.
Shin, S.-Y., Kim, T., Lee, H.-S., Kang, J., Lee, J., Cho, K.-H., and Kim, D. (2014). The switching role of β-adrenergic receptor signalling in cell survival or death decision of cardiomyocytes. Nat. Commun. *5*, 5777.
Sugihara, G., May, R., Ye, H., Hsieh, C., Deyle, E., Fogarty, M., and Munch, S. (2012). Detecting Causality in Complex Ecosystems. Science *338*, 496–500.
Symmons, O., and Raj, A. (2016). What's luck got to do with it? Single cells, multiple fates, and biological non-determinism. Mol. Cell *62*, 788–802.
Toné, S., Sugimoto, K., Tanda, K., Suda, T., Uehira, K., Kanouchi, H., Samejima, K., Minatogawa, Y., and Earnshaw, W.C. (2007). Three Distinct Stages of Apoptotic Nuclear Condensation Revealed by Time-Lapse Imaging, Biochemical and Electron Microscopy Analysis of Cell-Free Apoptosis. Exp. Cell Res. *313*, 3635–3644.
Tsai, C.-Y., Kuo, W.-W., Shibu, M.A., Lin, Y.-M., Liu, C.-N., Chen, Y.-H., Day, C.-H., Shen, C.-Y., Viswanadha, V.P., and Huang, C.-Y. (2017). E2/ER β inhibit ISO-induced cardiac cellular hypertrophy by suppressing Ca2+-calcineurin signaling. PLOS ONE *12*, e0184153.
Venables, W.N., and Ripley, B.D. (2002). Modern Applied Statistics with S (New York: Springer-Verlag).
Vidal, M., Wieland, T., Lohse, M., and Lorenz, K. (2012). β-Adrenergic receptor stimulation causes cardiac hypertrophy via a Gβγ/Erk-dependent pathway. Cardiovasc. Res. *96*, 255–264.
Vilela, M., and Danuser, G. (2011). What's wrong with correlative experiments? Nat Cell Biol *13*, 1011–1011.
Wang, L., Brugge, J.S., and Janes, K.A. (2011). Intersection of FOXO- and RUNX1-mediated gene expression programs in single breast epithelial cells during morphogenesis and tumor progression. Proc. Natl. Acad. Sci. U. S. A. *108*, E803–E812.
Wencker, D., Chandra, M., Nguyen, K., Miao, W., Garantziotis, S., Factor, S.M., Shirani, J., Armstrong, R.C., and Kitsis, R.N. (2003). A mechanistic role for cardiac myocyte apoptosis in heart failure. J. Clin. Invest. *111*, 1497–1504.
Wickham, H., Averick, M., Bryan, J., Chang, W., McGowan, L., François, R., Grolemund, G., Hayes, A., Henry, L., Hester, J., et al. (2019). Welcome to the Tidyverse. J. Open Source Softw. *4*, 1686.

Wlodkowic, D., Skommer, J., and Darzynkiewicz, Z. (2009). Flow cytometry-based apoptosis detection. Methods Mol. Biol. Clifton NJ *559*.

Woo, L.A., Tkachenko, S., Ding, M., Plowright, A.T., Engkvist, O., Andersson, H., Drowley, L., Barrett, I., Firth, M., Akerblad, P., et al. (2019). High-content phenotypic assay for proliferation of human iPSC-derived cardiomyocytes identifies L-type calcium channels as targets. J. Mol. Cell. Cardiol. *127*, 204–214.

Yang, J., Polanowska-Grabowska, R., Smith, J., Shields, C., and Saucerman, J. (2013). PKA catalytic subunit compartmentation regulates contractile and hypertrophic responses to β-adrenergic signaling. J. Mol. Cell. Cardiol. *66C*, 83–93.

Yue, T.L., Wang, C., Romanic, A.M., Kikly, K., Keller, P., DeWolf, W.E., Hart, T.K., Thomas, H.C., Storer, B., Gu, J.L., et al. (1998). Staurosporine-induced apoptosis in cardiomyocytes: A potential role of caspase-3. J. Mol. Cell. Cardiol. *30*, 495–507.

Zaugg, M., Xu, W., Lucchinetti, E., Shafiq, S.A., Jamali, N.Z., and Siddiqui, M.A. (2000). Beta-adrenergic receptor subtypes differentially affect apoptosis in adult rat ventricular myocytes. Circulation *102*, 344–350.

Supplemental Figures

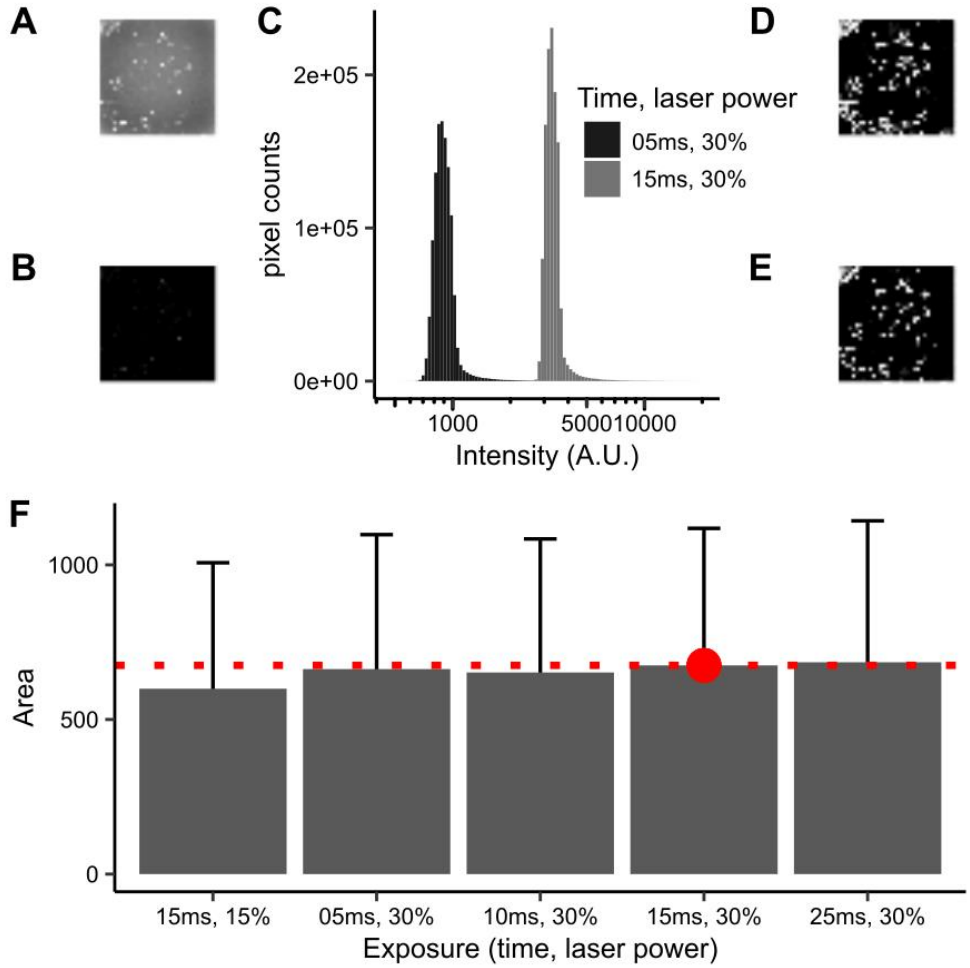

Supplemental Figure 1. Segmentation on eGFP fluorescence probability maps is robust to 5-fold variation in signal-to-noise ratio.
The same field of view of cells was taken with either 15 ms (A) or 5 ms (B) of exposure with 30% laser power.
(C) Image intensity histogram of the two images. The same Ilastik random forest model was used to generate GFP fluorescence probability maps of the images taken with either 15 ms (D) or 5ms (E) of exposure.
(F) Single-cell area distributions were compared with varying signal-to-noise ratios generated by varying exposure duration or laser power.

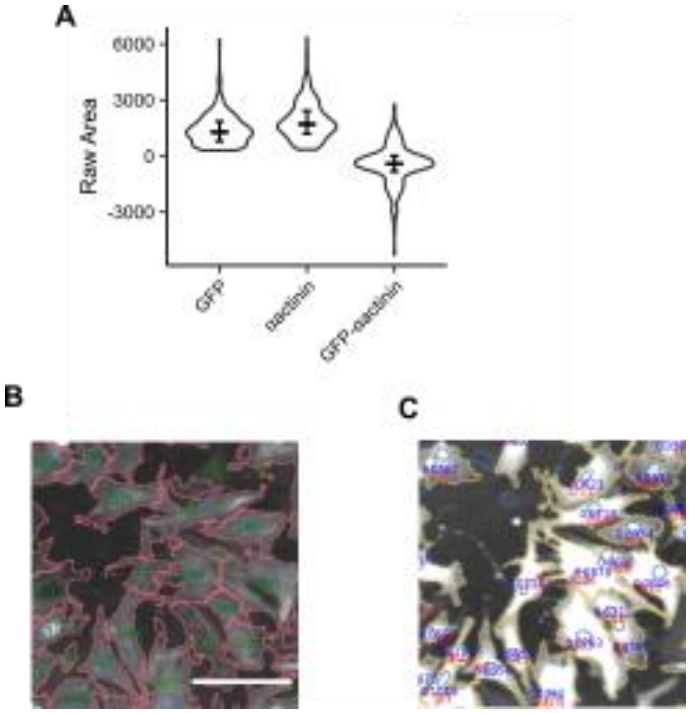

Supplemental Figure 2. GFP watershed algorithm provides better fidelity to actual cell areas

(**A**) Areas of GFP and α-actinin double-positive cells segmented in GFP or α-actinin channels, and the difference between the two. Solid lines indicate population median, error bars indicate interquartile range.

Segmentation borders of α-actinin (**B**,red) or GFP (**C**, yellow) fluorescence. Green numbers in (**B**) or red numbers in (**C**) indicate cell areas. Blue numbers in (**C**) indicate GFP fluorescence intensity.

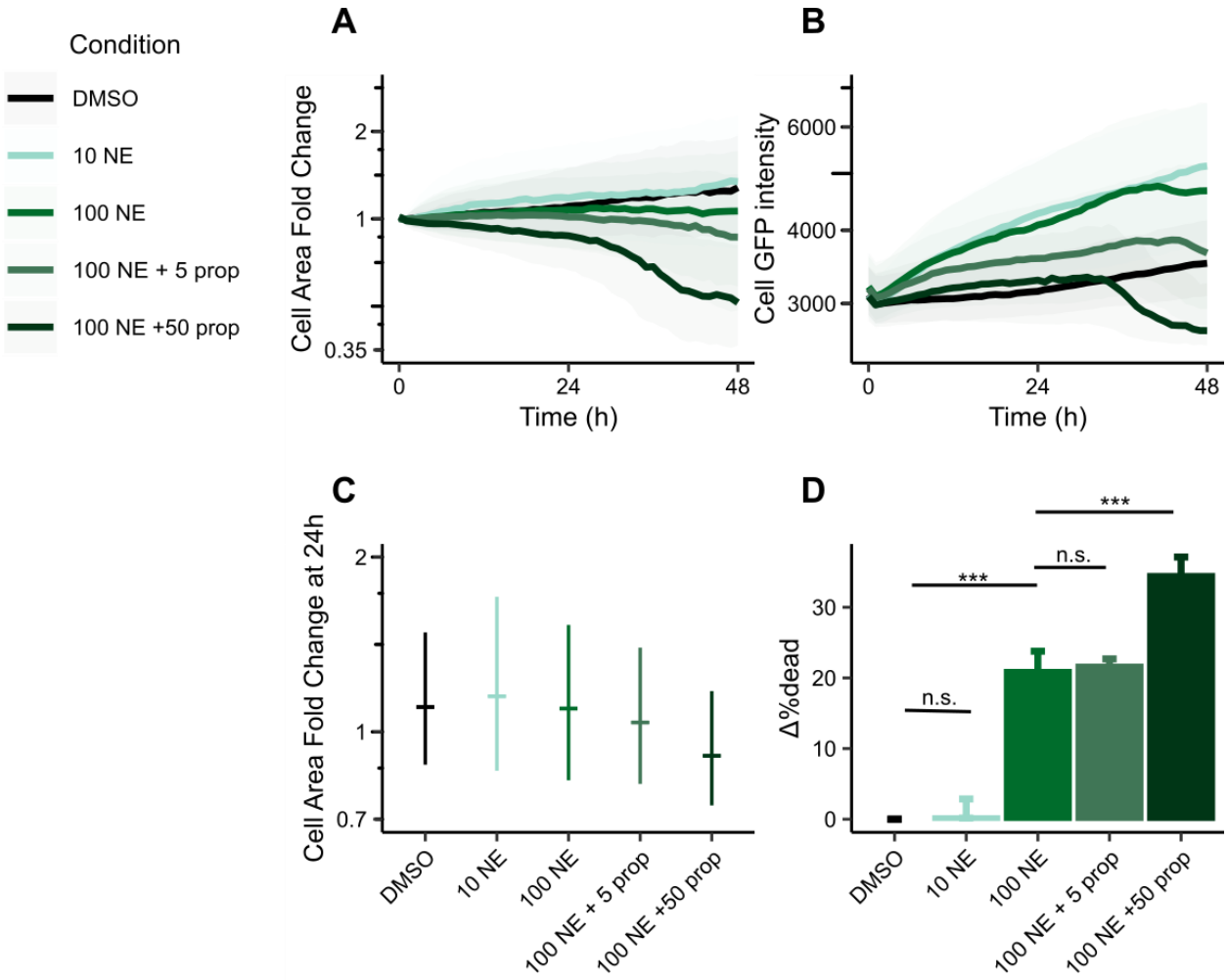

Supplemental Figure 3. Norepinephrine induces apoptosis that cannot be inhibited by propranolol.

48h hypertrophy (**A**) or eGFP (**B**) dynamics. Shaded area represents interquartile range. (**C**) Single-cell hypertrophy responses at 24 h. Solid lines indicate population median, errorbars indicate interquartile range.

(**D**) A5 binding response across 48 h. ***p ≤0.00026; mixed effects ANOVA followed by multiple comparisons of means with user-defined contrasts with Benjamini-Hochberg correction, n = 2 independent cell isolations

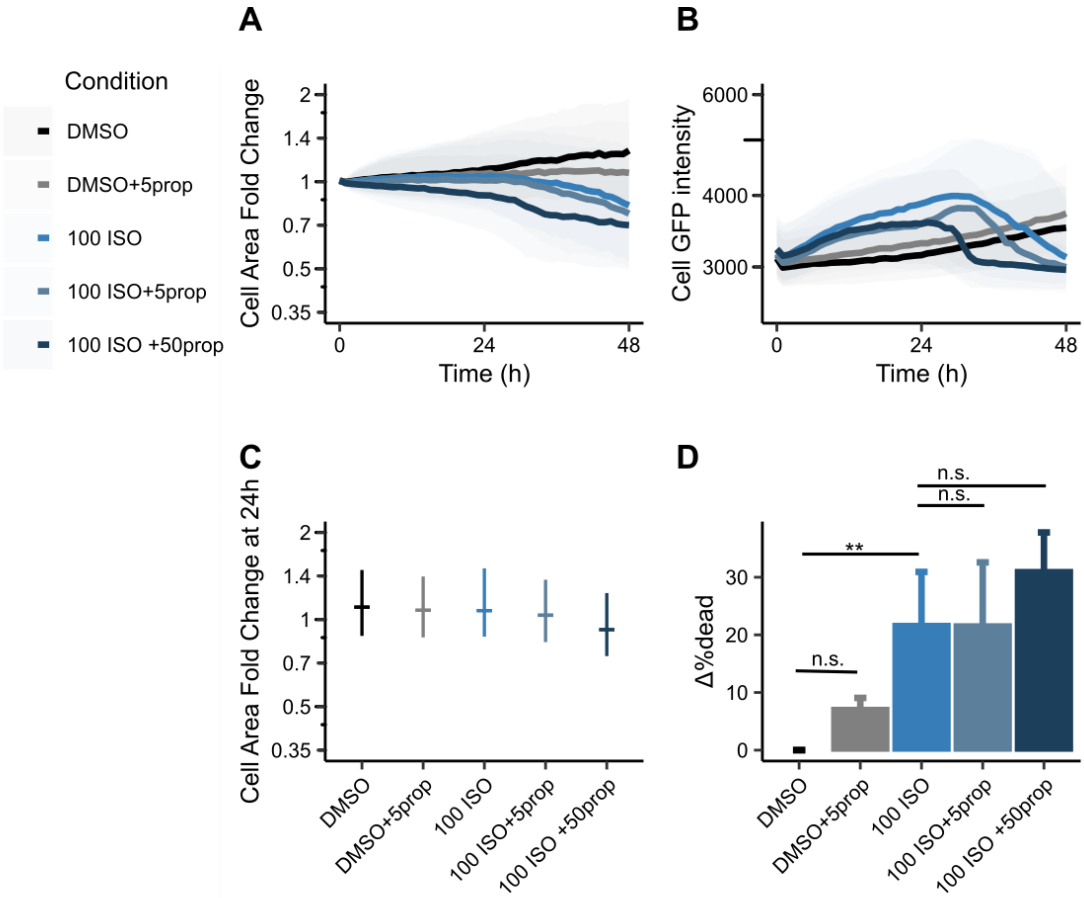

854

855 **Supplemental Figure 4. Propranolol does not inhibit ISO-induced apoptosis.**
856 48h hypertrophy (**A**) or eGFP (**B**) dynamics. Shaded area represents interquartile range.
857 (**C**) Single-cell hypertrophy responses at 24 h. Solid lines indicate population median, errorbars
858 indicate interquartile range.
859 (**D**) A5 binding response across 48 h. **p = 0.0033; mixed effects ANOVA followed by multiple
860 comparisons of means with user-defined contrasts with Benjamini-Hochberg correction, n = 2
861 independent cell isolations.
862

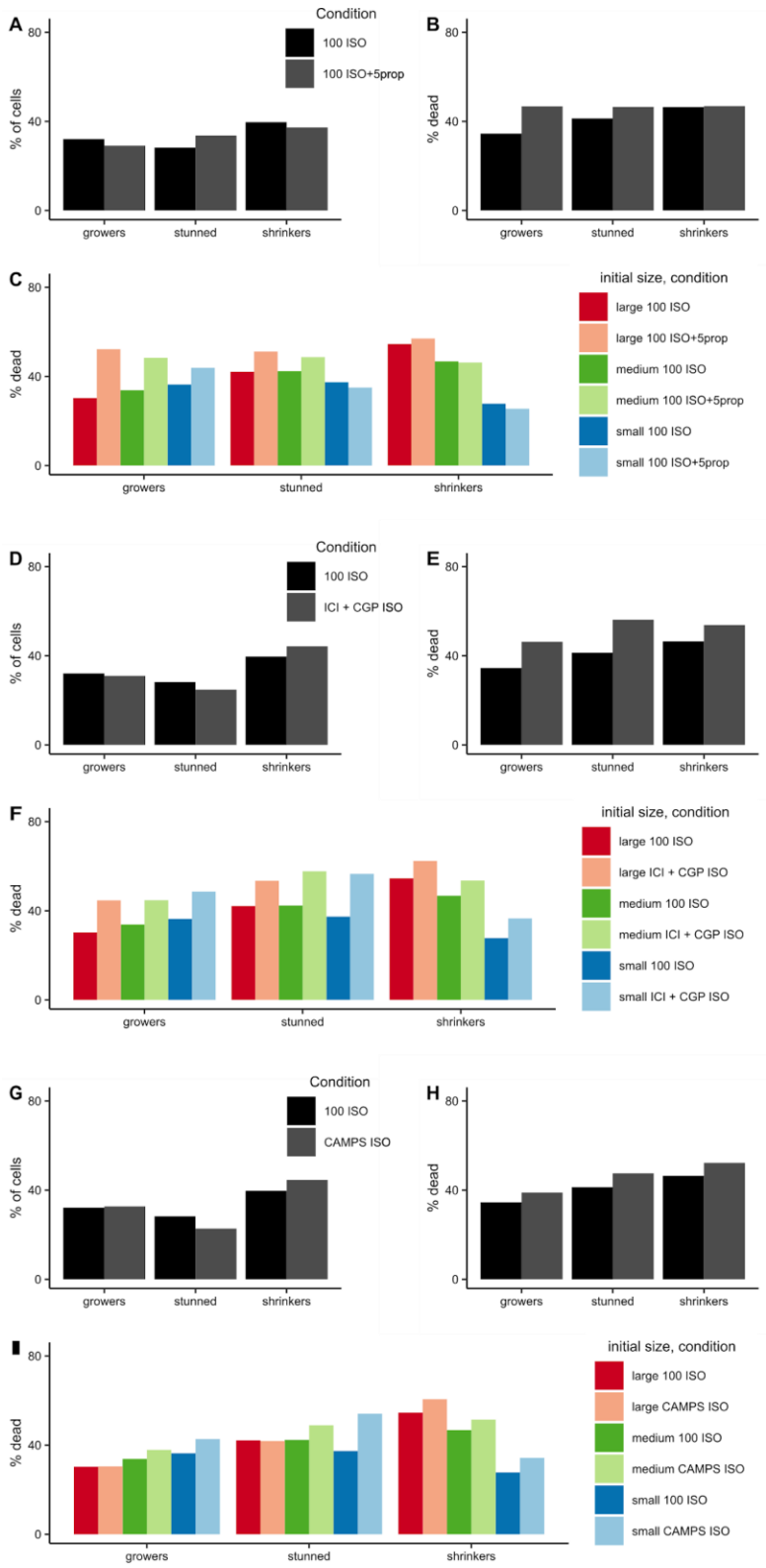

Supplemental Figure 5. βA signaling inhibitors increase ISO-induced apoptosis and proportion of stunned/shrinker subpopulations.

(**A, D, G**) Addition of βA signaling inhibitors (5 μM propranolol; 300 nM ICI-118,551 and 300

867 nM CGP 20712; or 100 μM Rp-cAMP) increase stunned or shrinker subpopulations.
868 (**B, E, H**) Addition of βA signaling inhibitors increase death rates of each growth subpopulation.
869 (**C, F, I**) Addition of βA signaling inhibitors increase death rates of each combination of growth
870 subpopulation and initial cell size, with the exception of the small initial cell size
871 stunned/shrinkers treated with propranolol (**C**).
872
873

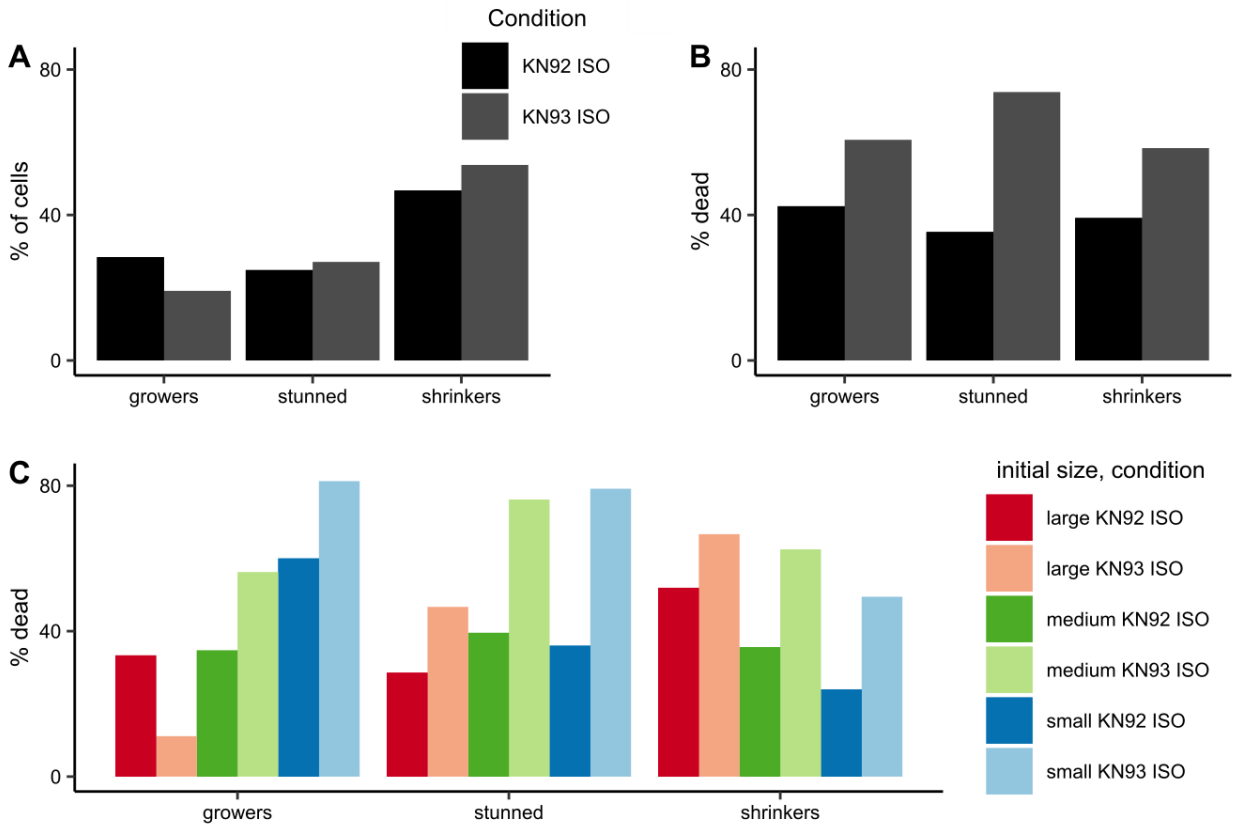

874
875 **Supplemental Figure 6. CaMKII inhibitors increase ISO-induced apoptosis.**
876 (**A**) Addition of 1 μM CaMKII inhibitor KN-93 increases proportion of shrinker subpopulation
877 compared to the addition of 1 μM of KN-92, a KN-93 analogue lacking CaM kinase activity.
878 (**B**) Addition of KN-93 increases death rates of each growth subpopulation.
879 (**C**) Addition of Kn-93 increases death rates of medium and small cells across all growth
880 subpopulations.
881

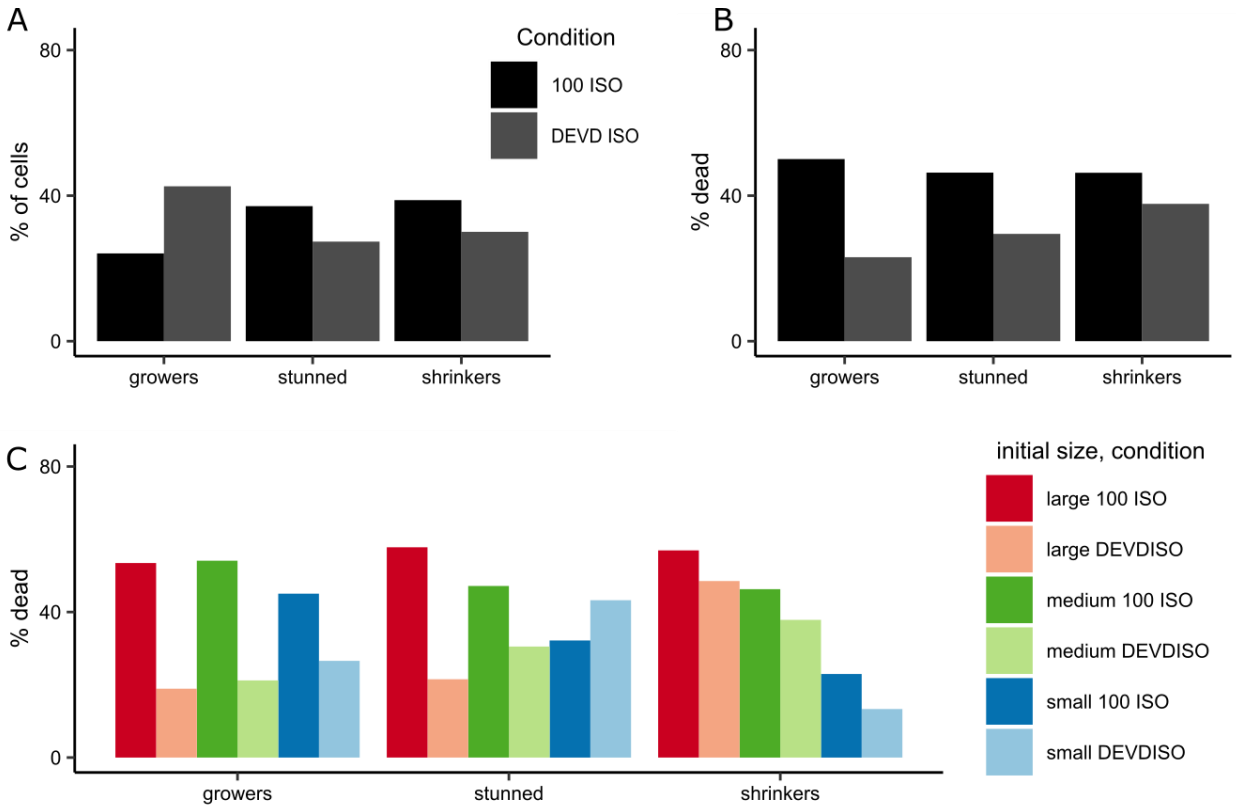

Supplemental Figure 7. Z-DEVD-FMK inhibits ISO-induced apoptosis and increases grower cell subpopulation.
(**A**) Addition 20 μM Z-DEVD-FMK increases the proportion of grower cells while decreasing the proportion of shrinker cells.
(**B**) Addition of Z-DEVD-FMK decreases the death rates of each growth subpopulation.
(**C**) Addition of Z-DEVD-FMK decreases the death rates of each growth subpopulation except for initially-small, stunned growth subpopulation.

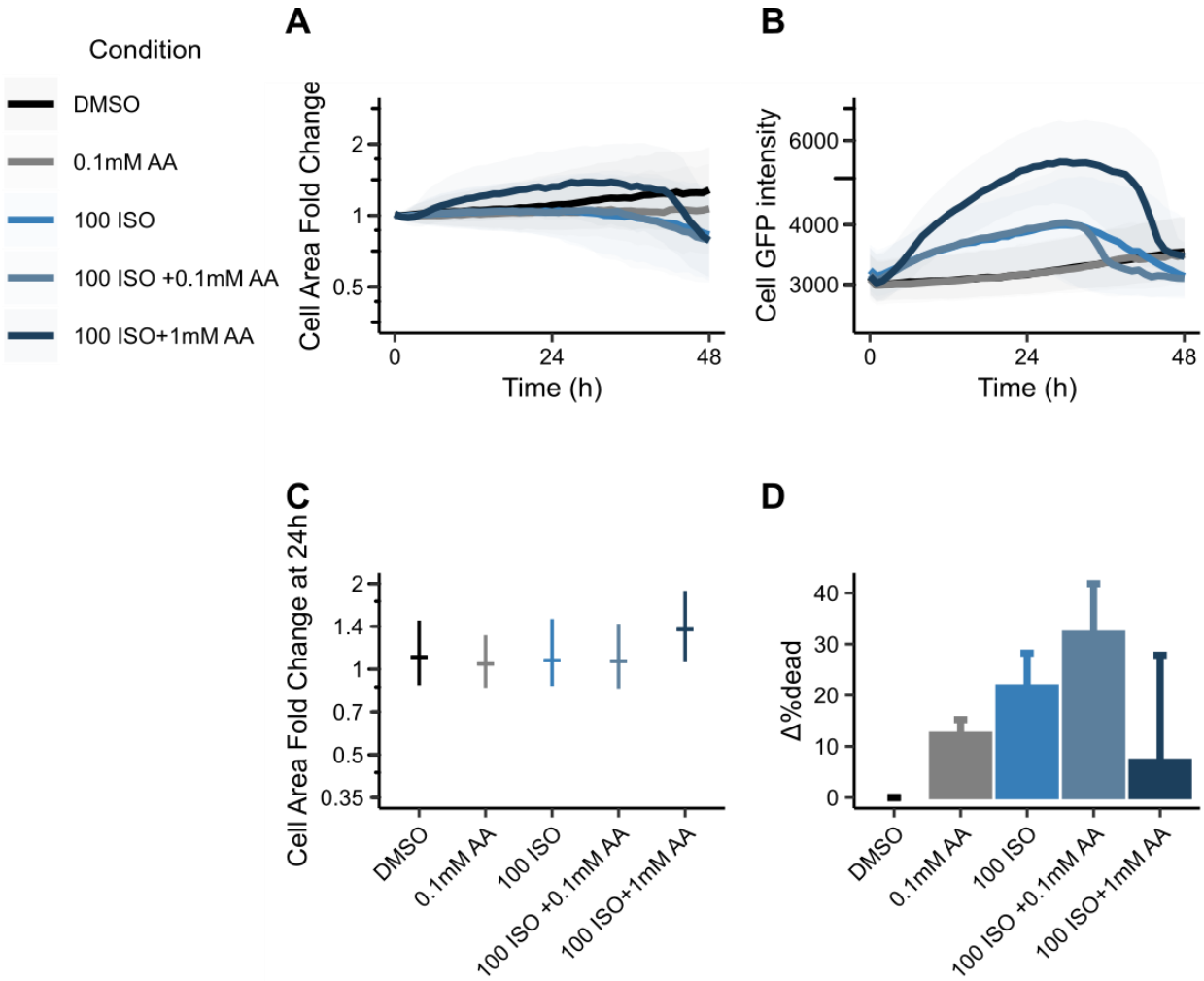

Supplemental Figure 8. Ascorbic acid may protect against isoproterenol-induced apoptosis.
48h hypertrophy (**A**) or eGFP (**B**) dynamics. Shaded area represents interquartile range. (**C**) Single-cell hypertrophy responses at 24 h. Solid lines indicate population median, errorbars indicate interquartile range.
(**D**) A5 binding response across 48 h. No significant differences across n = 2 independent cell isolations by mixed-effects ANOVA.

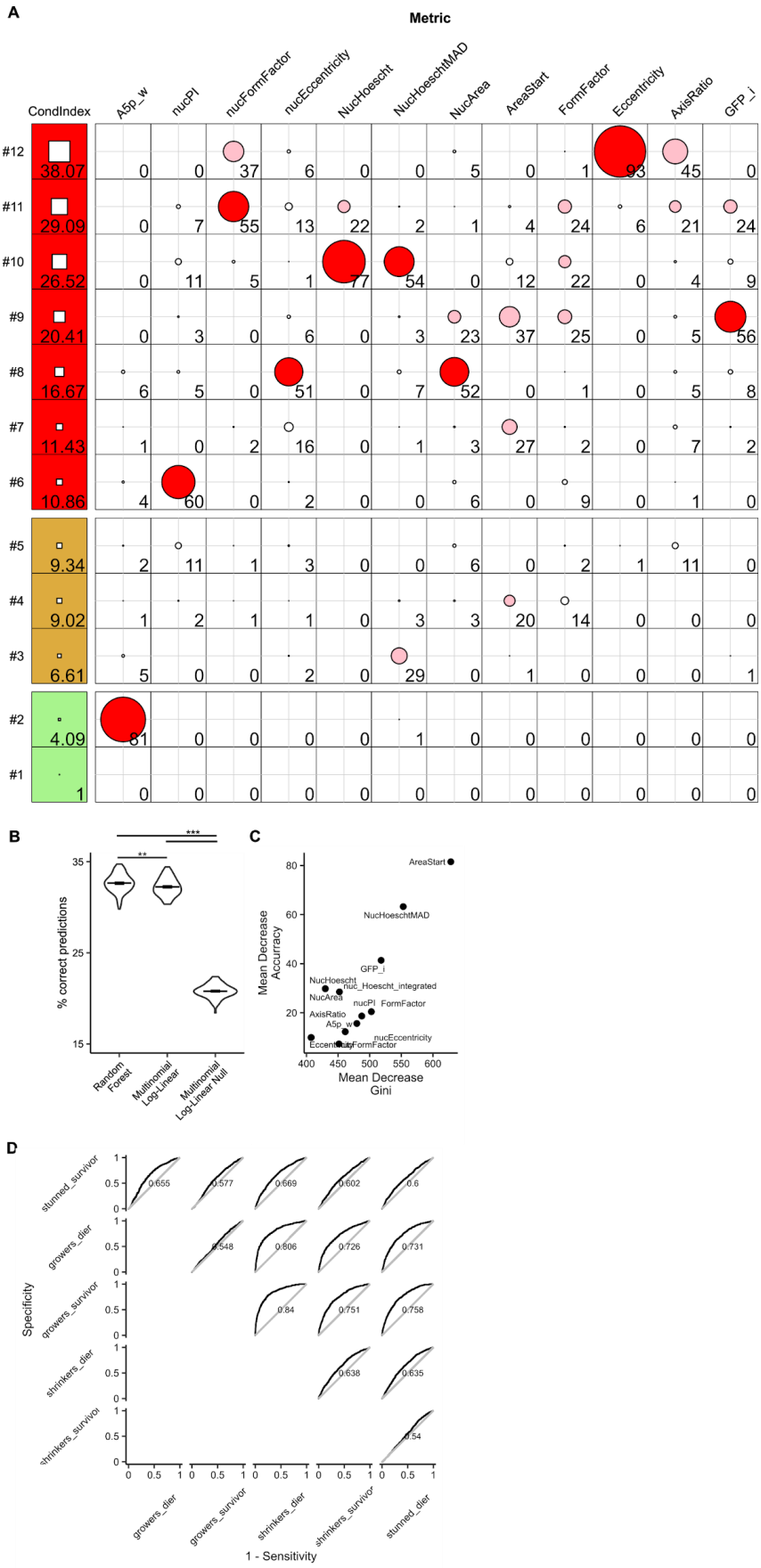
A
Metric
CondIndex
A5p_w
nucPI
nucFormFactor
nucEccentricity
NucHoescht
NucHoeschtMAD
NucArea
AreaStart
FormFactor
Eccentricity
AxisRatio
GFP_i
B
% correct predictions
Random Forest
Multinomial Log-Linear
Multinomial Log-Linear Null
C
Mean Decrease Accuracy
Mean Decrease Gini
AreaStart
NucHoeschtMAD
GFP_i
NucHoescht
nuc_Hoescht_integrated
NucArea
nucPI
FormFactor
AxisRatio
A5p_w
nucEccentricity
Eccentricity
D
Specificity
1 - Sensitivity
stunned_survivor
growers_dier
growers_survivor
shrinkers_dier
shrinkers_survivor
stunned_dier

Supplemental Figure 9. Colinearity of predictor variables and comparison of model performances.

(**A**) Tableplot of Condition indices and coefficient variance proportions (Friendly and Kwan, 2009). Briefly, condition indices represent scaled eigenvalues of the correlation matrix among the predictors variables. The condition index box is green for indexes less than 5, yellow if less than 10, and red if greater than 10. Each row represents an eigenvector with the "metric" columns corresponding to each predictor variable's proportion of variance scaled to 100.

(**B**) 5-fold cross validation accuracy. Error bars represent mean ± SEM. **p = 0.002, ***p < $2*10^{-22}$, repeated-measured ANOVA followed by paired T-test with Benjamini-Hochberg correction for multiple comparisons, n=100 random partitions.

(**C**) Random forest predictor variable importance measures.

(**D**) Multiclass and pairwise AUC curves.

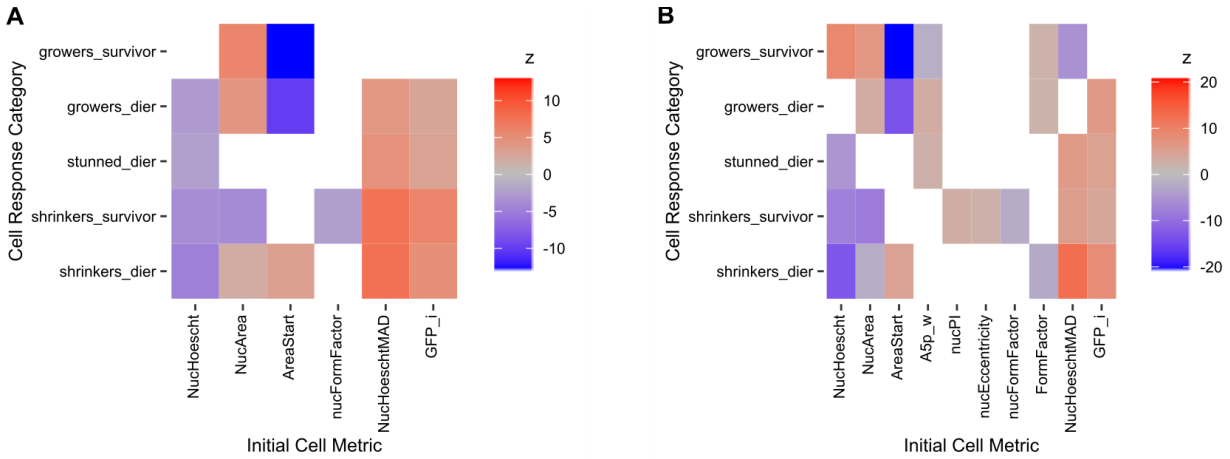

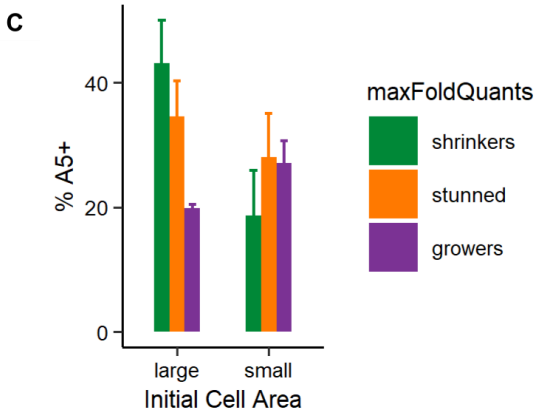

Supplemental Figure 10. Multinomial log-linear model coefficients for PE and 56.2 µM ISO.

(**A**) Model for 50 µM PE.

(**B**) Model for 56.2 µM ISO.

(**B**) Apoptosis rate by initial cell area and growth trajectory.

Supplemental Tables

Supplemental Table 1. **Multinomial log-linear regressions predicting hypertrophy-apoptosis phenotype likelihood relative to the stunned_survivor phenotype.** Values are represented as the regression coefficients and standard errors in parentheses. Akaike Information Criterion = 30818.4

	Dependent variable:				
	growers_die r	growers_survivo r	shrinkers_die r	shrinkers_survivo r	stunned_die r
	(1)	(2)	(3)	(4)	(5)
A5p_w	-0.247	-0.601***	-0.089	-0.108	0.058
	(0.200)	(0.173)	(0.178)	(0.166)	(0.194)
nucPI	0.615	0.326	2.405***	1.310**	0.313
	(0.648)	(0.572)	(0.552)	(0.538)	(0.636)
nucFormFactor	0.566	-0.159	0.433	-0.679*	0.553
	(0.452)	(0.372)	(0.397)	(0.365)	(0.439)
nucEccentricity	-0.160	-0.201	0.471*	0.369	0.552*

	(0.313)	(0.265)	(0.282)	(0.265)	(0.311)
NucHoescht	-0.162	2.559***	-11.594***	-7.476***	-5.250***
	(0.889)	(0.762)	(0.853)	(0.789)	(0.896)
NucHoeschtMAD	1.540*	-4.929***	14.391***	8.033***	8.553***
	(0.786)	(0.688)	(0.717)	(0.666)	(0.763)
NucArea	2.486***	2.450***	-1.229*	-3.251***	0.570
	(0.725)	(0.588)	(0.632)	(0.586)	(0.700)
AreaStart	-9.710***	-7.923***	4.959***	2.037***	0.750
	(0.685)	(0.532)	(0.461)	(0.452)	(0.531)
FormFactor	0.802***	0.685***	-0.017	0.151	0.311
	(0.309)	(0.265)	(0.275)	(0.262)	(0.301)
Eccentricity	0.018	0.277	0.220	-0.099	-0.104
	(0.404)	(0.345)	(0.364)	(0.336)	(0.392)

AxisRatio	-1.123	-0.701	-0.443	0.357	-0.034
	(0.792)	(0.634)	(0.629)	(0.572)	(0.694)
GFP_i	4.564***	-0.182	5.490***	2.564***	4.590***
	(0.718)	(0.688)	(0.640)	(0.633)	(0.697)
Constant	-1.182	1.363*	-2.813***	1.057	-3.031***
	(0.903)	(0.769)	(0.802)	(0.745)	(0.882)

Note: *p<0.1;>**p<0.05; ***p<0.01